The Astrophysical Journal, 758:59 (21pp), 2012 October 10 doi:10.1088/0004-637X/758/1/59

NEUTRON-POOR NICKEL ISOTOPE ANOMALIES IN METEORITES

Robert C. J. Steele[1,2,3], Christopher D. Coath[1], Marcel Regelous[1,4], Sara Russell[2], and Tim Elliott[1]
[1] Bristol Isotope Group, School of Earth Sciences, University of Bristol, Wills Memorial Building, Queen's Road, Bristol BS8 1RJ, UK; r.steele@uclmail.net
[2] Meteoritics and Cosmic mineralogy, The Natural History Museum, Cromwell Road, London SW7 5BD, UK
Received 2011 December 9; accepted 2012 July 27; published 2012 September 26

ABSTRACT

We present new, mass-independent, Ni isotope data for a range of bulk chondritic meteorites. The data are reported as $\varepsilon^{60}Ni_{58/61}$, $\varepsilon^{62}Ni_{58/61}$, and $\varepsilon^{64}Ni_{58/61}$, or the parts per ten thousand deviations from a terrestrial reference, the NIST SRM 986 standard, of the $^{58}Ni/^{61}Ni$ internally normalized $^{60}Ni/^{61}Ni$, $^{62}Ni/^{61}Ni$, and $^{64}Ni/^{61}Ni$ ratios. The chondrites show a range of 0.15, 0.29, and 0.84 in $\varepsilon^{60}Ni_{58/61}$, $\varepsilon^{62}Ni_{58/61}$, and $\varepsilon^{64}Ni_{58/61}$ relative to a typical sample precision of 0.03, 0.05, and 0.08 (2 s.e.), respectively. The carbonaceous chondrites show the largest positive anomalies, enstatite chondrites have approximately terrestrial ratios, though only EH match Earth's composition within uncertainty, and ordinary chondrites show negative anomalies. The meteorite data show a strong positive correlation between $\varepsilon^{62}Ni_{58/61}$ and $\varepsilon^{64}Ni_{58/61}$, an extrapolation of which is within the error of the average of previous measurements of calcium-, aluminium-rich inclusions. Moreover, the slope of this bulk meteorite array is 3.003 ± 0.166 which is within the error of that expected for an anomaly solely on ^{58}Ni. We also determined to high precision ($\sim$10 ppm per AMU) the mass-dependent fractionation of two meteorite samples which span the range of $\varepsilon^{62}Ni_{58/61}$ and $\varepsilon^{64}Ni_{58/61}$. These analyses show that "absolute" ratios of $^{58}Ni/^{61}Ni$ vary between these two samples whereas those of $^{62}Ni/^{61}Ni$ and $^{64}Ni/^{61}Ni$ do not. Thus, Ni isotopic differences seem most likely explained by variability in the neutron-poor ^{58}Ni, and not correlated anomalies in the neutron-rich isotopes, ^{62}Ni and ^{64}Ni. This contrasts with previous inferences from mass-independent measurements of Ni and other transition elements which invoked variable contributions of a neutron-rich component. We have examined different nucleosynthetic environments to determine the possible source of the anomalous material responsible for the isotopic variations observed in Ni and other transition elements within bulk samples. We find that the Ni isotopic variability of the solar system cannot be explained by mixing with a component of bulk stellar ejecta from either SN II, Wolf–Rayet or, an asymptotic giant branch source and is unlikely to result from bulk mixing of material from an SN Ia. However, variable admixture of material from the Si/S zone of an SN II can create all the characteristics of Ni isotope variations in solar system materials. Moreover, these characteristics can also be provided by an SN II with a range of masses from 15 to 40 $M_{\odot}$, showing that input from SN II is a robust source for Ni isotope variations in the solar system. Correlations of Ni isotope anomalies with O, Cr, and Ti isotope ratios and Pb/Yb in bulk meteorites suggest that the heterogeneous distribution of isotopic anomalies in the early solar system likely resulted from nebular sorting of chemically or physically different materials bearing different amounts of isotopes synthesized proximally to the collapse of the protosolar nebula.

Key words: astrochemistry – meteorites, meteors, meteoroids – methods: analytical – nuclear reactions, nucleosynthesis, abundances – protoplanetary disks

Online-only material: color figures, machine-readable table

1. INTRODUCTION

The discovery of isotopic anomalies in neutron-rich isotopes of Ca (Lee et al. 1978; Jungck et al. 1984) and iron group elements, e.g., Ti (Heydegger et al. 1979; Niemeyer & Lugmair 1980; Niederer et al. 1980) in calcium-, aluminium-rich inclusions (CAIs), was interpreted as strong evidence of heterogeneous input to the early solar system of material from a highly neutron-enriched supernova source. However, debate over the origin and circumstances of this event has continued and been added to by the discovery of mass-independent anomalies in bulk samples as well as CAIs. The progenitor of this neutron-rich component has been hypothesized to be a Type Ia supernova (SN Ia; e.g., Nomoto 1982; Hartmann et al. 1985; Meyer et al. 1996; Woosley 1997), a Type II supernova (SN II; e.g., Hartmann et al. 1985), or an asymptotic giant branch (AGB; e.g., Lugaro et al. 2004). It is likely that the source of the isotopic heterogeneity observed in early solar system materials is derived from the most recent nucleosynthetic event and therefore this heterogeneity may contain information about the birth environment of the Sun.

When attempting to identify sources of isotopic heterogeneity in the solar system, an important consideration resulting from the greatly differing isotopic compositions produced in different nucleosynthetic environments is the need to consider the possibility of effects on all the isotopes of the studied element. The majority of isotopic anomalies in meteorites are reported as mass-independent ratios that are normalized to an isotope ratio thought not to contain anomalies. This normalization removes the effects of mass-dependent fractionation, both natural and instrumental, which otherwise obscure potentially subtle source-related anomalies. However, the highly anomalous isotope ratios produced by stellar nucleosynthesis are not necessarily limited to a single isotope. Moreover, for some elements,

[3] Now at Department of Earth and Space Sciences, University of California Los Angeles (UCLA), Los Angeles, CA 90095–1567, USA.
[4] Now at GeoZentrum Nordbayern, Universität Erlangen-Nürnberg, Schlossgarten 5, D-91054 Erlangen, Germany.

Table 1
Mass-dependent and Mass-independent Ni Isotope Data, Reported Relative to NIST SRM 986, for Chondrites and Terrestrial Materials

	Group	NHM No.	n	n_{64}	$\varepsilon^{60}Ni_{58/61}$	2 s.e.	$\varepsilon^{62}Ni_{58/61}$	2 s.e.	$\varepsilon^{64}Ni_{58/61}$	2 s.e.	$\delta^{60/58}Ni$	2 s.e.
Carbonaceous chondrites												
Orgueil[+]	CI	1985, M148	4	4	−0.008	0.010	0.203	0.031	0.585	0.089	0.185	0.024
Leoville[+]	CV	1919, 144	8	8	−0.107	0.011	0.061	0.028	0.135	0.076	0.300[a]	0.050
Allende[+]	CV	...	4	4	−0.098	0.016	0.131	0.019	0.324	0.036	...	...
NWA-801[+]	CR	...	5	5	−0.157	0.015	0.116	0.022	0.361	0.065	...	...
Felix[+]	CO	1919, 89	4	4	−0.079	0.030	0.097	0.029	0.262	0.107	0.310[a]	0.070
Murchison[+]	CM	1988, M23	4	4	−0.098	0.028	0.124	0.033	0.298	0.092	0.210[a]	0.030
Cold-Bokkeveld[+]	CM	13989	4	4	−0.084	0.020	0.113	0.050	0.335	0.105	...	...
Ordinary chondrite												
Dhurmsala	LL	...	4	4	−0.049	0.027	−0.085	0.011	−0.210	0.059	...	...
Chainpur[+]	LL	1915, 86	8	8	−0.054	0.017	−0.065	0.036	−0.171	0.102	0.280[a]	0.100
Tieschitz[+]	HL	1975, M11	8	8	−0.052	0.019	−0.080	0.036	−0.253	0.048	...	...
Tenham	L	...	4	4	−0.026	0.020	−0.057	0.025	−0.117	0.135	...	...
Barratta	L	...	4	4	−0.042	0.022	−0.028	0.027	−0.105	0.073	...	...
Ceniceros	H	...	4	4	−0.063	0.010	−0.050	0.028	−0.078	0.102	...	...
Butsura	H	...	28	28	−0.048	0.008	−0.053	0.014	−0.171	0.033	...	...
Enstatite chondrite												
Khairpur[+]	EL	51366	4	4	−0.023	0.023	−0.054	0.028	−0.049	0.064	...	...
St. Mark's[+]	EH	1990, 339	4	4	−0.017	0.014	0.039	0.039	0.113	0.067	...	...
Abee[+]	EH	992, M7	4	4	−0.007	0.023	0.027	0.058	0.084	0.071	0.190[a]	0.050
Terrestrial standards												
NIST SRM 361	T	...	72	41	−0.011	0.007	0.029	0.013	0.136	0.033	−0.039	0.032
NIST SRM 986-col	T	...	4	4	0.002	0.006	−0.024	0.028	0.000	0.042	...	...
PtYG	T	...	20	20	0.010	0.008	−0.009	0.017	0.012	0.033	−0.645	0.080
JP-1	T	...	58	50	−0.006	0.007	0.035	0.010	0.117	0.021	0.100	0.080
DTS-2	T	...	4	4	−0.007	0.032	0.038	0.063	0.161	0.100	0.128	0.080
Bulk silicate Earth	T	...	...	...	−0.006	0.007	0.036	0.010	0.119	0.021	0.179	0.036

Notes. [a]Mass-dependent $\delta^{60/58}Ni$ data published by Cameron et al. (2009). [+]Meteorite samples dissolved and initially processed by Regelous et al. (2008); before analysis, these solutions were passed through anionic exchange resin (see Steele et al. 2011) in order to remove residual Zn. NIST SRM 361 and JP-1 have been processed both by Regelous et al. (2008) and during this study. The estimate for the bulk silicate Earth (BSE) is taken from Steele et al. (2011).

the choice of normalizing isotopes has been influenced by the assumption of neutron-rich isotope anomalies (e.g., Birck & Lugmair 1988). This makes the existence of anomalies on neutron-rich isotopes a point of interpretation as they may equally reside on the neutron-poor isotopes. This problem can be tackled in two ways. First and most obvious, is to determine the location of anomalies by determining the "absolute" isotope ratios (e.g., Niederer et al. 1985). Where only small anomalies exist, such as in bulk samples, this may be very analytically challenging. The second approach is to consider nucleosynthetic contributions to all isotopes without making the assumption that any one ratio is unaffected. In these two ways, robust information about the nucleosynthetic origins of the solar system can be obtained from isotopic analyses of early solar system materials.

As an iron group element, Ni has a relatively high abundance in the solar system. It also exhibits moderately refractory, moderately siderophile behavior, and so is a major constituent of most meteorites. Nickel has five stable isotopes which are produced with contrasting efficiencies in different nucleosynthetic environments, and so may provide valuable constraints on the stellar sources of the solar system. Moreover, two of the isotopes, ^{62}Ni and ^{64}Ni, are highly neutron-rich and so offer a good test of hypothesized input to the solar system from a high neutron density type Ia supernova (SN Ia; e.g., Nomoto 1982; Hartmann et al. 1985; Meyer et al. 1996; Woosley 1997). Nickel also has enough isotopes that the mass-dependent fractionation of samples can be determined by double spike analysis, meaning it may be possible to determine on which isotopes the anomalies reside. One isotope, ^{60}Ni, is the decay product of the short-lived ^{60}Fe ($t_{1/2} = 2.62$Ma; Rugel et al. 2009), so Ni isotope measurements of meteorites may also provide a constraint for the short-lived radionuclide budget of the early solar system. Therefore, Ni offers a tempting opportunity to study the nucleosynthetic sources of the materials that make up the solar system and how they were mixed in its earliest history.

2. RESULTS

Nickel isotope data from suite of seven carbonaceous chondrites (CCs), three enstatite chondrites, and seven ordinary chondrites (OCs) are presented, see Table 1. The methods used to collect these data are outlined in the Appendix and Steele et al. (2011). These data comprise measurements on both fully processed samples and previously separated Ni splits (Regelous et al. 2008) that have undergone additional processing to remove Zn for high-precision determination of ^{64}Ni. The data show a range of 0.15 ‰, 0.29 ‰, and 0.84 ‰ in $\varepsilon^{60}Ni_{58/61}$, $\varepsilon^{62}Ni_{58/61}$, and $\varepsilon^{64}Ni_{58/61}$, respectively, where $\varepsilon^{i}Ni_{58/61}$ is the parts per ten thousand (‰) difference in the $^{i}Ni/^{61}Ni$ ratio, internally normalized to $^{58}Ni/^{61}Ni$, relative to the NIST SRM 986 standard. There is a strong positive correlation between $\varepsilon^{62}Ni_{58/61}$ and $\varepsilon^{64}Ni_{58/61}$, Figure 1, which overlaps with that previously defined by measurements of iron meteorites (Steele et al. 2011). The combined data sets yield a slope of

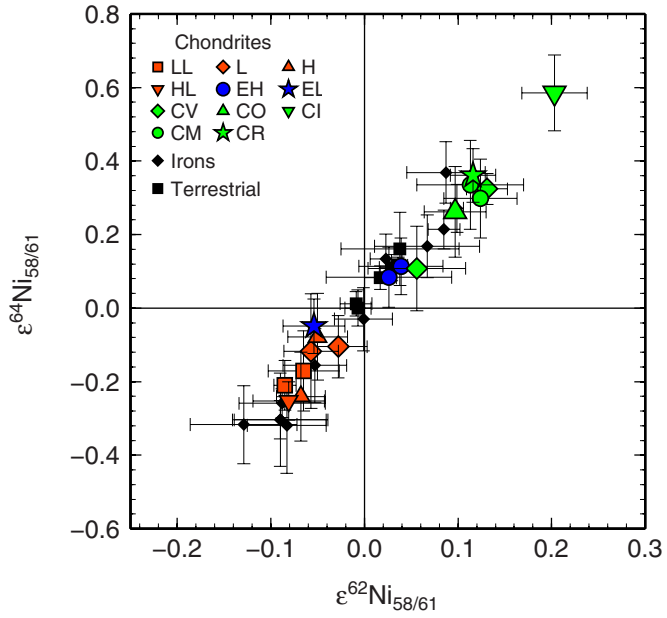

Figure 1. Strong positive correlation between $\varepsilon^{64}Ni_{58/61}$ and $\varepsilon^{62}Ni_{58/61}$ for chondrites which has a slope of 3.003 ±0.166, see the main text for regression details. Also shown are data for iron meteorites from Steele et al. (2011) which cover effectively the same range as the chondrites. Errors are 2 standard errors (2 s.e.).

(A color version of this figure is available in the online journal.)

3.003 ± 0.166 (MSWD = 1.021 and n = 215). This slope, uncertainty, and MSWD were determined by York regression (York 1969; Mahon 1996; York et al. 2004) using all 215 individual analyses of all 30 meteorite and peridotite samples, including iron meteorites from Steele et al. (2011). Tlacotepec was not used as it shows evidence of spallation (Steele et al. 2011). Uncertainties used in the regression were estimated from the entire data set (by the method described in Steele et al. 2011, and in the Appendix) and give values of 0.042 ‰ and 0.082 ‰ (1 standard deviation (1 s.d.) on a single analysis, compared to the 2 s.e. for the averaged analyses for given samples reported in Table 1) for $\varepsilon^{62}Ni_{58/61}$ and $\varepsilon^{64}Ni_{58/61}$, respectively, and a correlation coefficient of 0.68. Numerical simulations showed these 215 "raw" data provided a more accurate slope than regressions using averages and standard errors, see the Appendix. Notably, an extrapolation of this best-fit line intersects the compositions of the CAIs previously measured by Birck & Lugmair (1988), see Figure 2(a), suggesting that a common process produces the Ni isotopic variations in CAIs and bulk meteorites (see also Trinquier et al. 2009). The CCs have the highest positive anomalies in $\varepsilon^{62}Ni_{58/61}$ and $\varepsilon^{64}Ni_{58/61}$, enstatite chondrites have approximately terrestrial ratios, and the OCs exhibit negative anomalies. This pattern is the same as that observed in other neutron-rich nuclides, e.g., $\varepsilon^{54}Cr_{52/50}$ and $\varepsilon^{50}Ti_{49/47}$ (e.g., Shukolyukov & Lugmair 2006; Trinquier et al. 2007; Trinquier et al. 2009), resulting in correlated anomalies, see Figure 2(b). Of the CCs, Orgueil (CI) has the highest $\varepsilon^{62}Ni_{58/61}$ and $\varepsilon^{64}Ni_{58/61}$ ratios, which decrease through CV, CR, CM to CO. This order is consistent with that of $\varepsilon^{54}Cr_{52/50}$ (Figure 2(b)) but opposite to $\varepsilon^{50}Ti_{49/47}$, likely due to variable influence of CAIs on bulk Ti isotopic compositions (Trinquier et al. 2009). The iron meteorites reported by Steele et al. (2011) show essentially the same range in Ni isotopic compositions as the chondrites presented here. All CCs, OCs, and EL enstatite chondrites are resolved from the terrestrial composition and only EH enstatite chondrites are indistinguishable from the Earth in all mass-independent Ni isotope ratios. The latter are defined by analyses of natural terrestrial materials (e.g., the peridotites JP-1 and DTS-2) which yield $\varepsilon^{62}Ni_{58/61}$ 0.036 ‰ ± 0.010 ‰ and $\varepsilon^{64}Ni_{58/61}$ 0.119 ‰ ± 0.021 ‰, see Figure 1 (Steele et al. 2011). It should be noted that these samples differ slightly in their mass-independent Ni isotope ratios from the NIST SRM 986 reference. Steele et al. (2011) discuss this issue in detail and attribute this minor artifact to inaccuracies in the conventional approach of using a single exponential correction to account for instrumental and pre-analytical fractionation (see also Young et al. 2002). This should only significantly influence the moderately fractionated NIST SRM 986 composition and not those of our natural terrestrial or meteorite samples, which only show minor variability in their mass-dependent Ni isotopic compositions, see Table 1 (Steele et al. 2011; Cameron et al. 2009).

The relationship between $\varepsilon^{60}Ni_{58/61}$ and either $\varepsilon^{62}Ni_{58/61}$ (Figure 3) or $\varepsilon^{64}Ni_{58/61}$ (not shown) is more complex and has

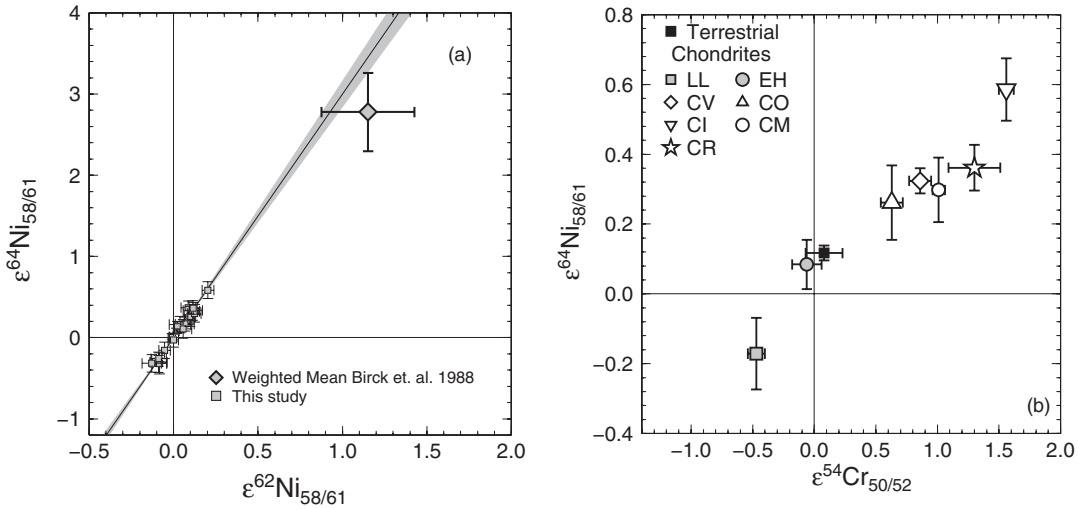

Figure 2. (a) York regression through the data from Figure 1 (solid curve, 2 s.e. in gray) is within the error of earlier CAI data from Birck & Lugmair (1988). The weighted mean of the Birck & Lugmair (1988) measurements with 2 s.e. error bars is also shown. (b) The correlation between $\varepsilon^{62}Ni_{58/61}$ and $\varepsilon^{54}Cr_{52/50}$, another neutron-rich iron group isotope thought to be produced in the same environment as ^{62}Ni and ^{64}Ni.

Table 2
High-precision Absolute Ratio Data for Orgueil (CI) and Butsura (OC)

	$\varepsilon^{58/61}$Ni	2 s.e.	$\varepsilon^{60/61}$Ni	2 s.e.	$\varepsilon^{61/61}$Ni	2 s.e.	$\varepsilon^{62/61}$Ni	2 s.e.	$\varepsilon^{64/61}$Ni	2 s.e.
Butsura	−3.00	0.22	−1.03	0.07	0.00	0.00	0.91	0.09	2.69	0.23
Orgueil	−2.17	0.25	−0.72	0.08	0.00	0.00	0.90	0.09	2.65	0.26

Note. Errors quoted include all sources of uncertainty discussed above, see Appendix A.3.2.

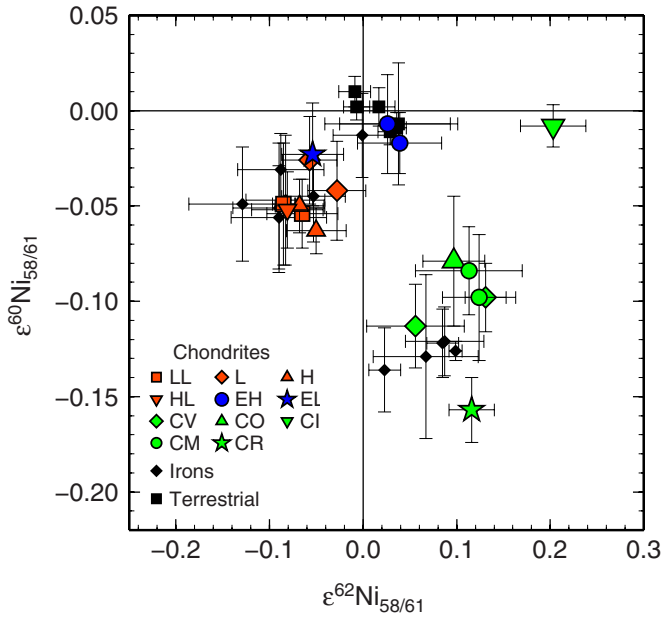

Figure 3. Plot showing $\varepsilon^{60}Ni_{58/61}$ vs. $\varepsilon^{62}Ni_{58/61}$. These data are consistent with the data of Regelous et al. (2008) but at slightly higher precision. No overall correlation exists, as discussed previously by Regelous et al. (2008).
(A color version of this figure is available in the online journal.)

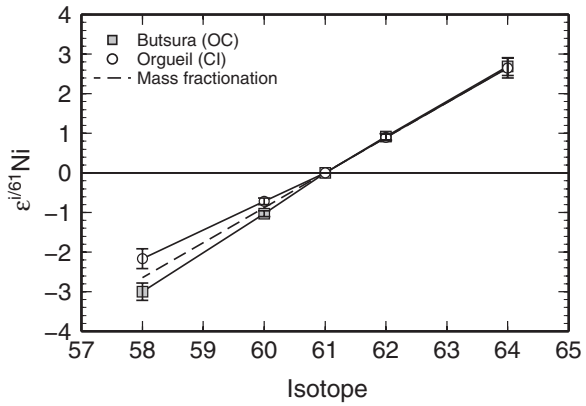

Figure 4. Absolute Ni isotope ratios, $^{i}Ni/^{61}Ni$, for Orgueil and Butsura in parts per ten thousand (‱) difference from NIST SRM 986. These data show strong evidence that Ni isotope heterogeneity is located on ^{58}Ni and ^{60}Ni and not on ^{62}Ni and ^{64}Ni.

been previously discussed by Regelous et al. (2008). Within the carbonaceous chondrites (CCs), there is a weak positive correlation between $\varepsilon^{60}Ni_{58/61}$ and $\varepsilon^{62}Ni_{58/61}$ that does not pass through terrestrial ratios, but is offset to positive $\varepsilon^{62}Ni_{58/61}$ or negative $\varepsilon^{60}Ni_{58/61}$. This trend is sequenced from high $\varepsilon^{60}Ni_{58/61}$ and $\varepsilon^{62}Ni_{58/61}$ in CI, through CO, CM, and CV to CR, which is different to the order of these groups in the $\varepsilon^{64}Ni_{58/61}$ versus $\varepsilon^{62}Ni_{58/61}$ array. The OCs have negative $\varepsilon^{60}Ni_{58/61}$ and, again, EH enstatite chondrites (ECs) have terrestrial ratios. Iron meteorites again span a similar range of $\varepsilon^{60}Ni_{58/61}$ as the chondrites, and only one iron meteorite sample, the IC iron meteorite Bendegó, is not resolved from terrestrial ratios (Steele et al. 2011).

2.1. Location of Anomalies

The slope of the meteorite array in $\varepsilon^{64}Ni_{58/61}$ versus $\varepsilon^{62}Ni_{58/61}$ (3.003 ± 0.166) is within the error of the slope of 2.96 predicted if anomalies were produced by variability in ^{58}Ni alone. This observation is worthy of investigation because variable ^{58}Ni anomalies are a simpler explanation than correlated variations on ^{62}Ni and ^{64}Ni. We note that variability on ^{58}Ni could be caused by interferences on this isotope during analysis, but we have extensively discussed and eliminated this possibility in a previous contribution (Steele et al. 2011).

To test the hypothesis that there are anomalies on ^{58}Ni, we have determined to high precision the "absolute ratios" of two chondrites, CI-type CC Orgueil and the H-type ordinary chondrite (OC) Butsura, which span the range of $\varepsilon^{62}Ni_{58/61}$ and $\varepsilon^{64}Ni_{58/61}$ anomalies. This has been achieved by coupling mass-independent measurements with high-precision, mass-dependent data determined by double spiking (see the Appendix), using a technique developed from Cameron et al. (2009). These results are shown in Table 2 and Figure 4 as ‱ difference of each isotope normalized to ^{61}Ni and NIST SRM 986. As is evident in Figure 4, the dominant character of the two samples is a general positive slope, indicating significant mass fractionation between the samples and the reference standard NIST SRM 986 (see Steele et al. 2011). Deviations from the dashed line, however, reflect the more subtle mass-independent anomalies.

While the $^{62}Ni/^{61}Ni$ and $^{64}Ni/^{61}Ni$ ratios are identical within error in these two meteorites, differences in $^{58}Ni/^{61}Ni$ are well resolved. The absolute ratios also show that a small anomaly remains on ^{60}Ni. These data are strong evidence that the anomalies in internally normalized Ni isotope ratios are in fact due to anomalies on the neutron-poor isotope ^{58}Ni (and ^{60}Ni) and not the neutron-rich isotopes ^{64}Ni and ^{62}Ni.

2.2. Normalization

Given our new inference that the anomalies in Ni reside on ^{58}Ni, we further present our data normalized to $^{62}Ni/^{61}Ni$ in Figures 5(a) and (b). Using this normalization, there is broadly correlated variation between $\varepsilon^{58}Ni_{62/61}$ and $\varepsilon^{60}Ni_{62/61}$, but there is still a small offset between the arrays of the CCs and OCs, and the EC and terrestrial samples, respectively. As expected, there is very little variation in $\varepsilon^{64}Ni_{62/61}$, with almost all of the data being within error of zero. We note that the slope of the data in $\varepsilon^{60}Ni_{62/61}$ versus $\varepsilon^{58}Ni_{62/61}$ space is approximately one-half. This slope could result from a variable interference on mass 61, but this possibility can be ruled out because the required associated anti-correlation in $\varepsilon^{60}Ni_{62/61}$ versus $\varepsilon^{64}Ni_{62/61}$ is not present (not shown). We have also discussed in more detail

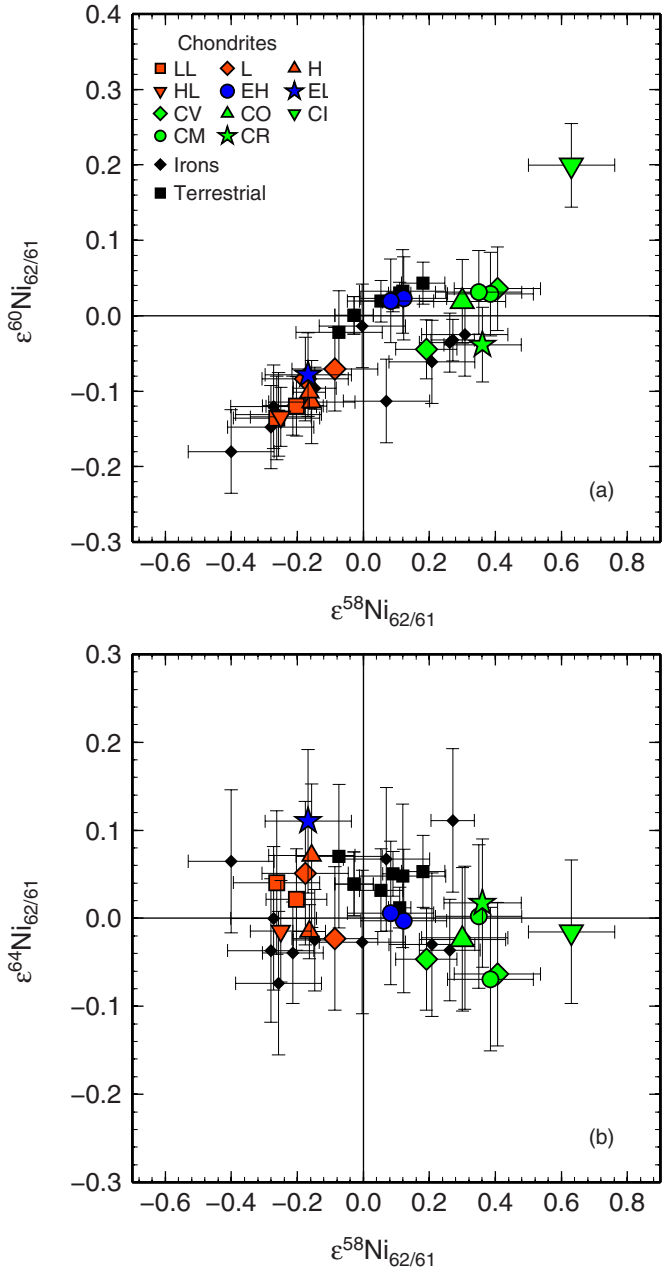

Figure 5. Plots showing the same data as presented in Figure 1 and Table 1 re-normalized to $^{62}Ni/^{61}Ni$.

(A color version of this figure is available in the online journal.)

elsewhere (Steele et al. 2011) the reasons we discount the possible presence of this type of interference in our analyses.

It is clearly useful to examine the data re-normalized to $^{62}Ni/^{61}Ni$, as presented in Figure 5, in order to most readily visualize the isotopic variations, but this may not necessarily be the most effective way of quantitatively analyzing our data. The $^{62}Ni/^{61}Ni$ normalization uses two minor isotopes with only one mass unit separation, which results in large propagated errors in the final mass-independent data. Therefore, in the rest of this study, we continue to use the $^{58}Ni/^{61}Ni$ ratio for normalization, which results in higher precision data. Moreover, existing work on mass-independent Ni isotope variations has already presented data normalized to two different ratios and a third, new, normalization would only add confusion. While it might initially seem obtuse to employ a scheme that uses a normalizing isotope ratio known to be strongly perturbed by nucleosynthetic effects, we emphasize that added nucleosynthetic components will likely influence all isotopes, albeit to different degrees. As long as potential anomalous contributions from all isotopes are considered in subsequent treatments, no problems will arise from the manner in which the data are reported.

3. DISCUSSION

3.1. Stellar Origin of Nucleosynthetic Heterogeneity

Given that previous measurements of CAIs (Birck & Lugmair 1988) lie on an extension of the Ni isotopic array defined by our bulk meteorite analyses, see Figure 2(a), variable proportions of a single anomalous component can potentially explain the solar system heterogeneity evident in $\varepsilon^{64}Ni_{58/61}$ versus $\varepsilon^{62}Ni_{58/61}$ plots. Since mass-independent anomalies in Ni are not thought to be generated within the solar system, the observed heterogeneity in compositions is likely the result of incomplete mixing, or "unmixing" of a common carrier phase. It is intriguing that the volatile-rich CI meteorites, which likely accreted beyond the snow line, are closer in composition to the highly refractory CAIs, thought to be formed closer to the sun than the other more volatile-poor bulk meteorites (e.g., OCs) that presumably represent material from intermediate nebula radii. The more prosaic explanation that the bulk meteorite Ni isotopic variability simply reflects variable proportions of CAIs in different meteorite groups is implausible, since CAIs are neither a volumetrically dominant component of most chondrites, nor a dominant repository of Ni. Moreover, no CAIs are found in the CI CC Orgueil, the bulk meteorite which has the closest isotopic composition to CAIs. Similar observations and inferences have been made for the isotope systematics of other iron group elements, e.g., Ti and Cr (Trinquier et al. 2009).

An initial objective is thus to identify the stellar origin of the component which occurs in different proportions within different meteorite types. We subsequently address the processes by which this material can be variably distributed across the solar system.

The elements of the iron abundance peak are dominantly produced in stars by nuclear statistical equilibrium (NSE), the e-process (Burbidge et al. 1957). The e-process is thought to occur in a range of stellar sources and these different nucleosynthetic environments can produce very large and contrasting isotope anomalies. Such nucleosynthetic components have isotopic anomalies many orders of magnitude larger than the total variation in the solar system. In order to assess the influence of adding such exotic material to mass-independent isotope ratios in the solar system, the contribution to all isotopes needs to be considered. Below, such a treatment is presented, which allows us to identify plausible nucleosynthetic components that can generate correlated variability in mass-independent isotopic ratios in solar system materials, such as shown in Figure 1.

A key aspect in our approach is accounting for nucleosynthetic perturbations of the normalizing isotope ratio. Solar system samples are corrected for natural and instrumental fractionation using the exponential law (Russell et al. 1978),

$$R^{j/i}_{\rm frac} = R^{j/i}_{\rm ref}\left(\frac{m_j}{m_i}\right)^{\beta}, \quad (1)$$

where β is the exponential fractionation factor, and $R^{j/i}_{\rm ref}$ and $R^{j/i}_{\rm frac}$ are the ratios of isotope j to isotope i in a reference material and a sample fractionated from that reference material. Two

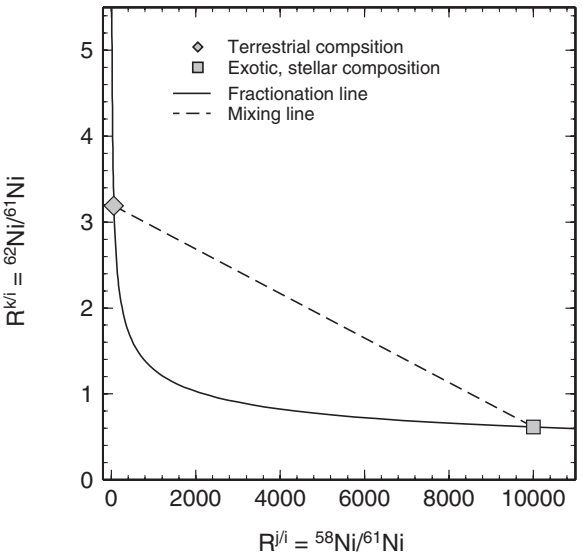

Figure 6. Plot showing the difference between the path of exponential fractionation and mixing in three isotope space at extreme ratios.

ratios, fractionated mass-dependently, e.g., $R^{k/i}$ and $R^{j/i}$, form an exponential relationship shown in Figure 6. If this passes through the bulk terrestrial composition, then it is the terrestrial fractionation line (TFL). If we take $R^{j/i}_{\rm ref}$ as our normalizing ratio, then a positive internally normalized mass-independent anomaly in $R^{k/i}$ is defined as deviation above the exponential law at constant $R^{j/i}_{\rm ref}$, and when presented as parts per ten thousand difference to a terrestrial standard, is written $\varepsilon^k R_{j/i}$.

In Figure 6, we show an isotopically extreme stellar component (square) which we have placed on the TFL for illustrative purposes. Positive mass-independent anomalies can be created by mixing this exotic stellar component with a terrestrial composition (diamond), since in this plot, where the two axes are ratios with common denominators, mixing defines a straight line and so always lies above the mass fractionation curve in this illustration. If we had erroneously normalized the composition of the exotic component to a terrestrial ^{58}Ni/^{61}Ni before calculating the effects of mixing, no anomaly would be apparent. The effects of mixing between solar and exotic compositions can be calculated for each isotope of interest and the resulting mixture suitably normalized to the conventional solar reference value, as discussed by Simon et al. (2009). However, we illustrate below that for a small amount of added material, the co-variation of two mass-independent isotope ratios of a given element can be calculated more readily.

At very small degrees of fractionation, the exponential law approximates to a straight line with a slope of $\ln(m_k/m_i)/\ln(m_j/m_i)$ as illustrated by the solid line in Figure 7(a). In this figure, the x-axis is the normalizing ratio, $\varepsilon^{58/61}$Ni, and the y-axis is the ratio to be normalized, $\varepsilon^{62/61}$Ni. Hence, the mass-independent ratio of a composition in this three-isotope space is equal to the vertical distance measured from the solid line. The dashed line in Figure 7(a) is the mixing line to a highly exotic nucleosynthetic composition at the point $(\varepsilon^{j/i}_{\rm nuc}R,\ \varepsilon^{k/i}_{\rm nuc}R)$. The difference in the slopes of these lines is given by

$$\Delta s^{k/i}_{j/i} = s_{\rm mix} - s_{\rm frac} = \left(\frac{\varepsilon^{k/i}_{\rm nuc}R}{\varepsilon^{j/i}_{\rm nuc}R}\right) - \left(\frac{\ln(m_k/m_i)}{\ln(m_j/m_i)}\right), \qquad (2)$$

where $\varepsilon^{k/i}_{\rm nuc}R$ and $\varepsilon^{j/i}_{\rm nuc}R$ are the compositions of a modeled nucleosynthetic environment. The second term on the right-hand side is the slope of fractionation by the exponential law, see Young et al. (2002). Figure 7(b) has k (= ^{62}Ni) replaced by l (= ^{64}Ni) but is otherwise identical to Figure 7(a). The corresponding expression for the difference in slopes, $\Delta s^{l/i}_{j/i}$, is similar to Equation (2).

If a small fraction of the exotic component is mixed into a nebula (with composition $\varepsilon = 0$), then the resulting composition of the mixture can be written as $\varepsilon^{x/i}_{\rm nuc}R \cdot f$, where f is the mixing parameter and x is j, k, or l. The resulting mass-independent isotope ratios of the mixture can be written in terms of the difference in the slopes, thus

$$\varepsilon^k R_{j/i} = \Delta s^{k/i}_{j/i}\left(\varepsilon^{j/i}_{\rm nuc}R \cdot f\right) \qquad (3)$$

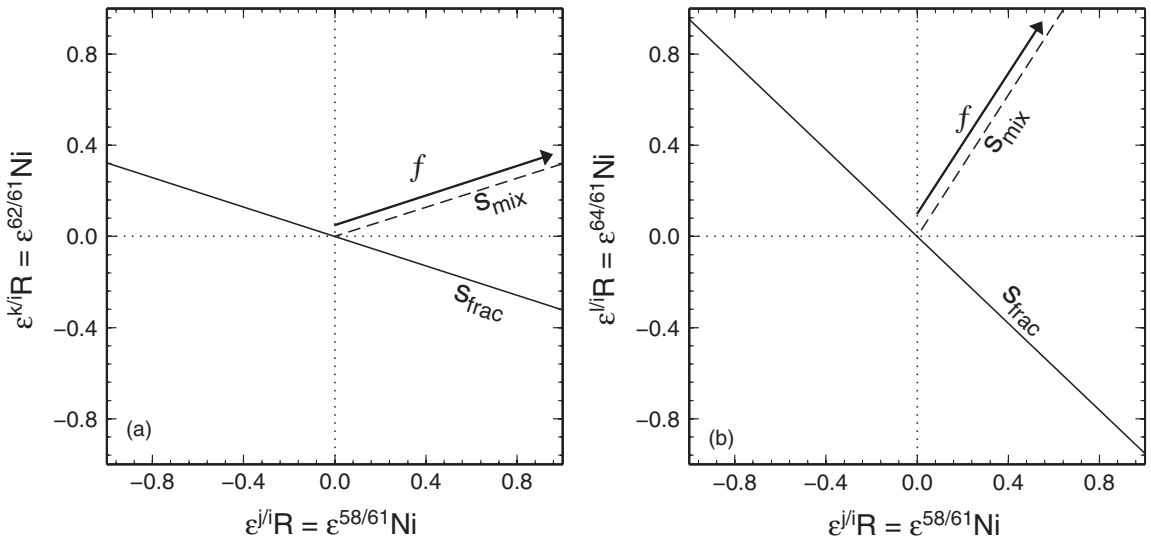

Figure 7. Schematic plots showing the difference between the path of exponential fractionation and mixing on three isotope plots. $s_{\rm frac}$ is the path of exponential fractionation given by the slope $\ln(m_x/m_i)/\ln(m_j/m_i)$, where x can be k or l, $s_{\rm mix}$ is the path of mixing between the average solar system composition and an anomalous nucleosynthetic composition, and f is the fraction of the distance along the mixing line from the origin to the anomalous end member.

and

$$\varepsilon^{l}R_{j/i} = \Delta s_{j/i}^{l/i}\left(\varepsilon_{\rm nuc}^{j/i}R \cdot f\right). \quad (4)$$

Dividing Equation (4) by Equation (3) yields

$$\varepsilon^{l}R_{j/i} = \frac{\Delta s_{j/i}^{l/i}}{\Delta s_{j/i}^{k/i}} \cdot \varepsilon^{k}R_{j/i}. \quad (5)$$

Hence, in a plot of $\varepsilon^{l}R_{j/i}$ versus $\varepsilon^{k}R_{j/i}$, mixtures will lie on a straight line with slope $\Delta s_{j/i}^{l/i}/\Delta s_{j/i}^{k/i}$.

Thus, for a system of four or more isotopes, the slope produced on a plot of two mass-independent isotope ratios can be calculated for the admixture of a small amount of exotic material to the solar system.

In the case of Ni, k and l may be any isotope of interest, for example, ^{64}Ni and ^{62}Ni, while j and i are once again the normalizing isotopes ^{58}Ni and ^{61}Ni. The ratio of the slopes, $\Delta s_{58/61}^{64/61}/\Delta s_{58/61}^{62/61}$, gives the slope of mixing between a terrestrial composition and an exotic component in relative normalized isotope space, e.g., $\varepsilon^{64}{\rm Ni}_{58/61}$ versus $\varepsilon^{62}{\rm Ni}_{58/61}$. The slopes obtained for different astrophysical environments can then be compared with the slope defined by anomalies in bulk meteorites. By finding slopes from nucleosynthetic environments that match those in the solar system array, it may be possible to identify the particular nucleosynthetic environment that created the component responsible for the Ni isotope variations in bulk meteorites. It must be stressed that it does not matter on which isotopes the anomalies reside, e.g., on ^{58}Ni or ^{62}Ni and ^{64}Ni, because this method includes all contributions from the normalizing and reported ratios.

In order to calculate such a slope for an element, two co-varying internally normalized ratios are required. This means there must be at least three independent isotope ratios, i.e., four isotopes. Of the existing data in the literature and this study, for Fe group transition elements, only Ti and Ni satisfy these conditions. Chromium has enough isotopes, but because of the decay of the abundant but variably distributed ^{53}Mn, initial values of ^{53}Cr are potentially masked by different radiogenic contributions. Due to chemical fractionation during transport from stellar sources or early solar system processing, inter-element slopes are unlikely to show original correlations. Since Ni is the primary objective of this study, fitting the Ni isotopes is our major criterion. However, the slope of the solar system array in Ti isotope space is also considered.

3.1.1. Application to Ni Isotopes

The isotopic composition of different bulk nucleosynthetic environments has been modeled by many studies. For SN Ia, we have used data from Woosley (1997), Travaglio et al. (2004), Iwamoto et al. (1999), Hashimoto (1995), and Maeda et al. (2010). For type II supernova (SN II), we have used data from Iwamoto et al. (1999), Umeda & Nomoto (2002), Nomoto et al. (1997), Rauscher et al. (2002), and Hashimoto (1995). We have used asymptotic giant branch star (AGB) models kindly provided by A. Davis (2009, private communication). The composition of material given off by Wolf–Rayet stars has been estimated using the wind from high-mass ($>35\,M_{\odot}$) supernova models of Rauscher et al. (2002). In Figure 8(a), we show the slopes that would be produced in $\varepsilon^{64}{\rm Ni}_{58/61}$ versus $\varepsilon^{62}{\rm Ni}_{58/61}$ by mixing the bulk ejecta from the sources modeled in the studies above with typical solar system material. For reference, these slopes are plotted against the ^{58}Ni/^{61}Ni of the bulk ejecta to further indicate the wide range of compositions produced in different stellar environments. The model slopes can be compared to that observed in solar system materials in Figure 1, shown as a dashed line in Figure 8(a). The mass-independent Ni isotopic variability seen in the solar system can thus be accounted for by the addition to the solar nebula of material derived from model sources that plot within the dotted lines of Figure 8(a). It is clear that in $\varepsilon^{64}{\rm Ni}_{58/61}$ versus $\varepsilon^{62}{\rm Ni}_{58/61}$ space, the majority of the nucleosynthetic environments (shown in Figure 8(a)) do not produce appropriate model slopes. There is one SN Ia model (C-DDT/def of Maeda et al. 2010) that could mix with the solar nebula to produce a slope within the error of that observed in solar system materials. In addition, one SN II model (S25 of Rauscher et al. 2002) differs by only 2.05σ from the slope observed in meteorites and is the only other model within 3σ so we shall include it in the discussion. Mixing of material from the two models of AGB stars and the estimates of the composition of material lost from Wolf–Rayet stars do not

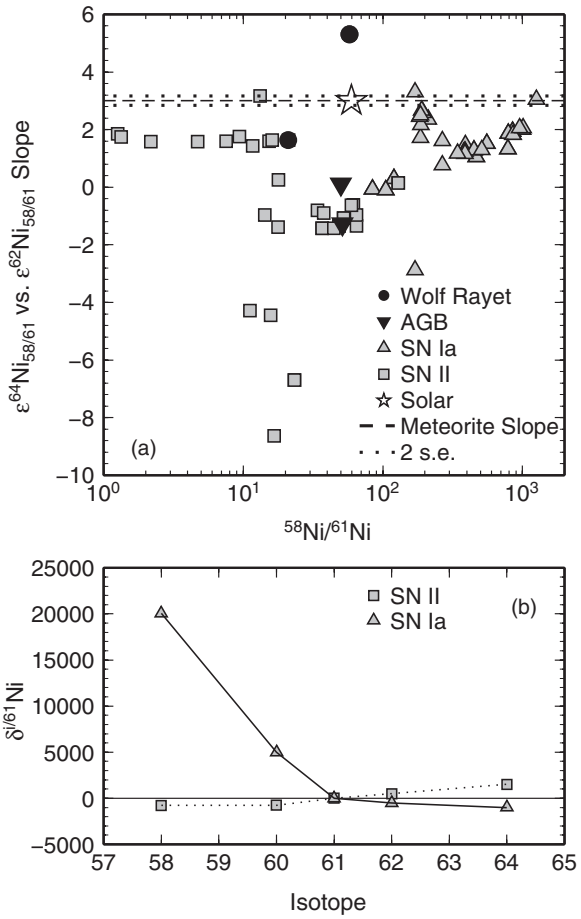

Figure 8. (a) Slope in $\varepsilon^{64}{\rm Ni}_{58/61}$ vs. $\varepsilon^{62}{\rm Ni}_{58/61}$ space that results from mixing exotic material from various astrophysical environments with typical solar system material. Models assume that all short-lived nuclides have decayed. We use data from Woosley (1997), Travaglio et al. (2004), Iwamoto et al. (1999), Hashimoto (1995), and Maeda et al. (2010) for SN Ia, Iwamoto et al. (1999), Umeda & Nomoto (2002), Nomoto et al. (1997), Rauscher et al. (2002), and Hashimoto (1995) for SN II, and A. Davis (2009, private communication) for AGB. The composition of material lost from Wolf–Rayet stars has been estimated using the wind from high-mass ($>35\,M_{\odot}$) supernova models of Rauscher et al. (2002). The dashed line indicates the slope observed in solar system materials, Figure 1, with 2 s.e. error (dotted lines). (b) The absolute ratios for the models (SN Ia (C-DDT/def of Maeda et al. 2010) and SN II model (S25 of Rauscher et al. 2002)) that match the slope observed in solar system materials.

produce an appropriate slope within the error of solar system materials.

As is shown above (Section 2.2), the anomalies in Ni isotopes likely reside on ^{58}Ni. Since our treatment of the modeled supernova compositions includes effects on all isotopes, those which match the slope in $\varepsilon^{64}Ni_{58/61}$ versus $\varepsilon^{62}Ni_{58/61}$ may do so either because ^{62}Ni and ^{64}Ni happen to be produced and mixed in with the correct abundances, or because the dominant isotope is ^{58}Ni. Therefore, we need to examine further the potentially successful solutions in Figure 8(a) to see if they are a result of the requisite ^{58}Ni enrichment. The results are shown in Figure 8(b), where the absolute Ni isotope ratios of the two models show that only the SN Ia model matches the slope by sole overproduction of ^{58}Ni. Since SN Ia nucleosynthesis is typically highly neutron enriched, however, the majority of SN Ia models do not match the meteorites slope. The only SN II model that matches the slope in $\varepsilon^{64}Ni_{58/61}$ versus $\varepsilon^{62}Ni_{58/61}$ does not have a ^{58}Ni anomaly; it matches the slope by chance overproduction of ^{62}Ni and ^{64}Ni in the correct proportions. Therefore, this SN II model cannot provide the observed Ni isotope heterogeneity to the solar system.

A further requirement for a plausible source of Ni isotope heterogeneity is that the same environment should be capable of producing other transition element isotope heterogeneity. One such element whose isotopic composition has recently been investigated in bulk samples by several studies is Ti (Leya et al. 2008, 2009; Trinquier et al. 2009). Like Ni, Ti exhibits a strong intra-element isotopic correlation between $\varepsilon^{50}Ti_{49/47}$ and $\varepsilon^{46}Ti_{49/47}$, while showing no variation in $\varepsilon^{48}Ti_{49/47}$ (Trinquier et al. 2009). Titanium isotope anomalies also correlate with Ni isotope anomalies, suggesting they may share a common source. Therefore, for the SN Ia model that produces an appropriate Ni component to account for solar system variability, it should similarly generate Ti of the correct isotopic composition to account for the slopes of the meteorite arrays in Ti isotope space.

The slope observed in solar system samples by Trinquier et al. (2009) between $\varepsilon^{50}Ti_{49/47}$ and $\varepsilon^{46}Ti_{49/47}$ is 5.48 ± 0.27, while the slopes for both $\varepsilon^{48}Ti_{49/47}$ versus $\varepsilon^{50}Ti_{49/47}$ and $\varepsilon^{48}Ti_{49/47}$ versus $\varepsilon^{46}Ti_{49/47}$ are zero. The supernova model that matches the Ni isotope constraints generates slopes in Ti of $\varepsilon^{50}Ti_{49/47}$ versus $\varepsilon^{46}Ti_{49/47} = -2.33$, $\varepsilon^{48}Ti_{49/47}$ versus $\varepsilon^{50}Ti_{49/47} = -3.9$, and $\varepsilon^{48}Ti_{49/47}$ versus $\varepsilon^{46}Ti_{49/47} = 0.6$. These clearly do not match those observed in meteorites and so cannot provide any supporting evidence that bulk ejecta from this unique SN Ia model can account for iron group isotopic variability in the solar system.

In summary, addition of bulk ejecta from an SN II cannot account for the Ni isotope heterogeneity to the solar system, while only a single SN Ia model can account for both the correct slope of meteoritic material in $\varepsilon^{62}Ni_{58/61}$, $\varepsilon^{64}Ni_{58/61}$ space by providing ^{58}Ni anomalies. However, one model is not a strong case for the source of Ni isotope heterogeneity. Moreover, this model cannot account for the heterogeneity in Ti isotopes observed by Trinquier et al. (2009), and so cannot account for Fe group isotope heterogeneity in general. Therefore, no calculated bulk supernova inputs seem appropriate to explain solar system variation so we further examine the compositions of individual nucleosynthetic shells within supernovae.

3.1.2. Supernova Components

Type Ia supernovae have three distinct components: a large ^{56}Ni core, a region of Fe abundance peak elements, and an outer region of lighter intermediate mass elements up to Ca (Kasen et al. 2009). Dynamical models of SN Ia explosions show that the inner regions consisting of the ^{56}Ni core and Fe group elements undergo Rayleigh–Taylor instabilities and are likely to be turbulently mixed (Kasen et al. 2009). This may suggest that bulk SN Ia are likely to give homogenized isotope ratios for iron group elements and that treatment beyond what we attempted in the last section is not warranted.

Conversely, SN II are explosions of much more massive stars, 3–70 $M_\odot$, so effective homogenization is less likely. Type II supernovae are normally split into eight zones named after the two most abundant elements (Meyer et al. 1995). Thus, we consider the isotope anomalies found from individual shells of SN II as in several recent studies (e.g., Dauphas et al. 2008; Moynier et al. 2009; Liu et al. 2009) and in established work on discrete pre-solar grains (e.g., Zinner 2003).

Rauscher et al. (2002) computed isotopic abundances for multiple spherical shells within an SN II for different events over a range of pre-supernova masses (15–40 $M_\odot$), see http://nucastro.org. These shells can be treated in the same way as the bulk supernova models discussed previously and the slope in mass-independent isotope space can be determined for variable mixing of a small amount of each shell into the solar system. For the same reason as discussed in Meyer et al. (1995), namely, a balance between galactic occurrence and mass ejected, we examine in detail a 25 $M_\odot$ supernova model. Other supernova masses have been examined and are referred to where relevant.

The production of Ni isotopes through a 25 $M_\odot$ SN II is shown in Figure 9(a), and the slopes produced by mixing this material into the solar system are shown in Figure 9(b). These figures illustrate that the addition of material from the Si/S zone of an SN II would produce the same slope in $\varepsilon^{64}Ni_{58/61}$ versus $\varepsilon^{62}Ni_{58/61}$ space as observed in the meteorite sample array. While only shown for a 25 $M_\odot$ SN II, it is interesting to note that the same is true for all other stellar masses, 15 $M_\odot$, 19 $M_\odot$, 20 $M_\odot$, 30 $M_\odot$, 35 $M_\odot$, and 40 $M_\odot$, modeled by Rauscher et al. (2002). Moreover, as seen in Figure 9(a), the Si/S zone also produces ^{58}Ni as the dominant Ni isotope—5 orders of magnitude higher than the next most abundant Ni isotope. Therefore, the Si/S zone meets all the criteria as the source of Ni isotope heterogeneity in the early solar system. In addition to the models of Rauscher et al. (2002), the compositions of different zones of a 25 $M_\odot$ SN II were computed by Meyer et al. (1995). The results of this independent model also show large overproduction of ^{58}Ni in the Si/S zone and produce the correct slope in $\varepsilon^{64}Ni_{58/61}$ versus $\varepsilon^{62}Ni_{58/61}$ (2.97) within the error of the slope of solar system material. The work of Meyer et al. (1995), therefore, provides supporting evidence that overproduction of ^{58}Ni in the Si/S zone is a general feature of SN II, making a robust case for SN II being the source of Ni isotope heterogeneity in the solar system.

The corresponding Ti isotope compositions of SN II shells and the slopes generated in mass-independent isotope plots as a result of mixing this material with the solar system are shown in Figures 9(c) and (d), respectively. The measurements of Trinquier et al. (2009) define a slope in $\varepsilon^{50}Ti_{49/47}$ versus $\varepsilon^{46}Ti_{49/47}$ space of 5.48 ± 0.27 and slopes of zero in $\varepsilon^{48}Ti_{49/47}$ versus $\varepsilon^{46}Ti_{49/47}$ and $\varepsilon^{48}Ti_{49/47}$ versus $\varepsilon^{50}Ti_{49/47}$. As can be seen from Figure 9(d), none of the individual zones match precisely the slopes observed in all three systems for solar system material. However, the upper section of the O/Ne zone is very close. This is an interesting finding, as from a qualitative consideration of the very different settings for dominant ^{46}Ti and ^{50}Ti production,

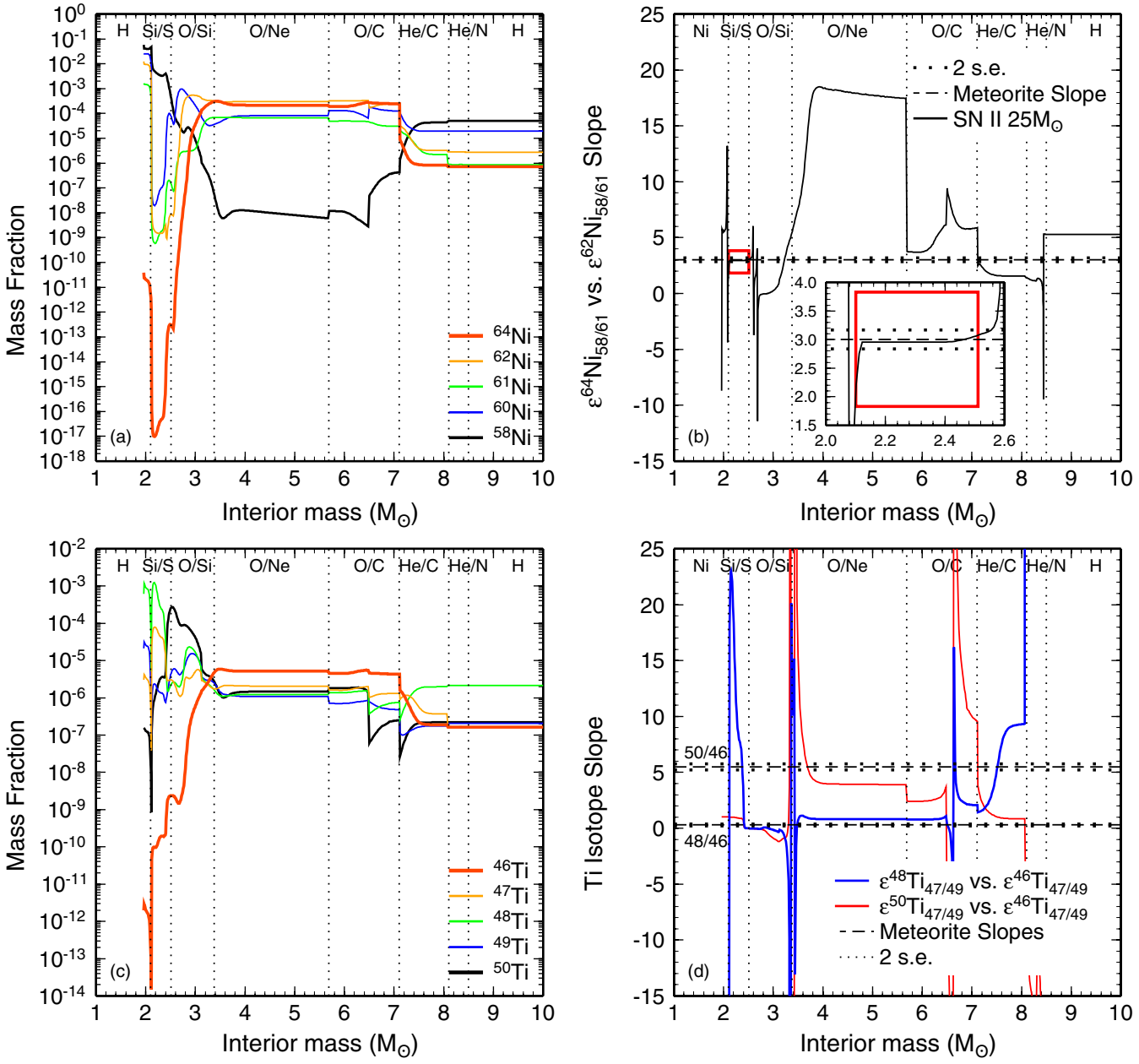

Figure 9. (a) Zonal yields of Ni isotopes from a 25 $M_{\odot}$ supernova from Rauscher et al. (2002). (b) The slope produced in $\varepsilon^{64}Ni_{58/61}$ vs. $\varepsilon^{62}Ni_{58/61}$ space by incomplete mixing of small amounts of these zones into the solar system, inset is an expanded view of the Si/S zone. See the text for details. (c) The zonal yields of Ti isotopes through a 25 $M_{\odot}$ supernova also from Rauscher et al. (2002). (d) The slope produced in $\varepsilon^{50}Ti_{49/47}$ vs. $\varepsilon^{46}Ti_{49/47}$, and $\varepsilon^{48}Ti_{49/47}$ vs. $\varepsilon^{46}Ti_{49/47}$ isotope space. Also shown in both diagrams are the names of the zones given by the two most abundant elements, after Meyer et al. (1995). These diagrams show that incompletely mixing material from the Si/S zone into the early solar system would produce the slope observed in Ni isotopes in the bulk meteorite materials. Though shown for the 25 $M_{\odot}$ supernova only, this is true of all the Rauscher et al. (2002) supernova models.

(A color version of this figure is available in the online journal.)

Trinquier et al. (2009) inferred that the correlated solar system anomalies must result from the contributions of several stellar components. This study did not consider the potential effects on normalizing isotopes, nor did a subsequent discussion by Leya et al. (2009). Therefore, the observation that a single source could account for all Ti isotopic variability recorded in meteorites is a notable result.

As discussed above, the more anomalies a nucleosynthetic environment can explain the more robust the case for it providing the source of isotope heterogeneity in the early solar system. Therefore, it is significant that a single SN II can provide the Ni and Ti anomalies observed in the solar system. However, it cannot be ignored that the Ti isotope anomalies that match solar system materials are not found in the same zones as those that produce appropriate Ni isotope compositions. On face value, this implies that the SN II is an unlikely source of solar system isotope heterogeneity, but it may be possible to decouple isotope anomalies of different elements. For example, different shells may produce condensates with dramatically different chemical or physical properties. Thus, processing during transport in the interstellar medium or within the solar system may generate isotopic anomalies by differential processing of pre-solar grains with radically different isotopic compositions. We consider scenarios in more detail in Section 3.3.

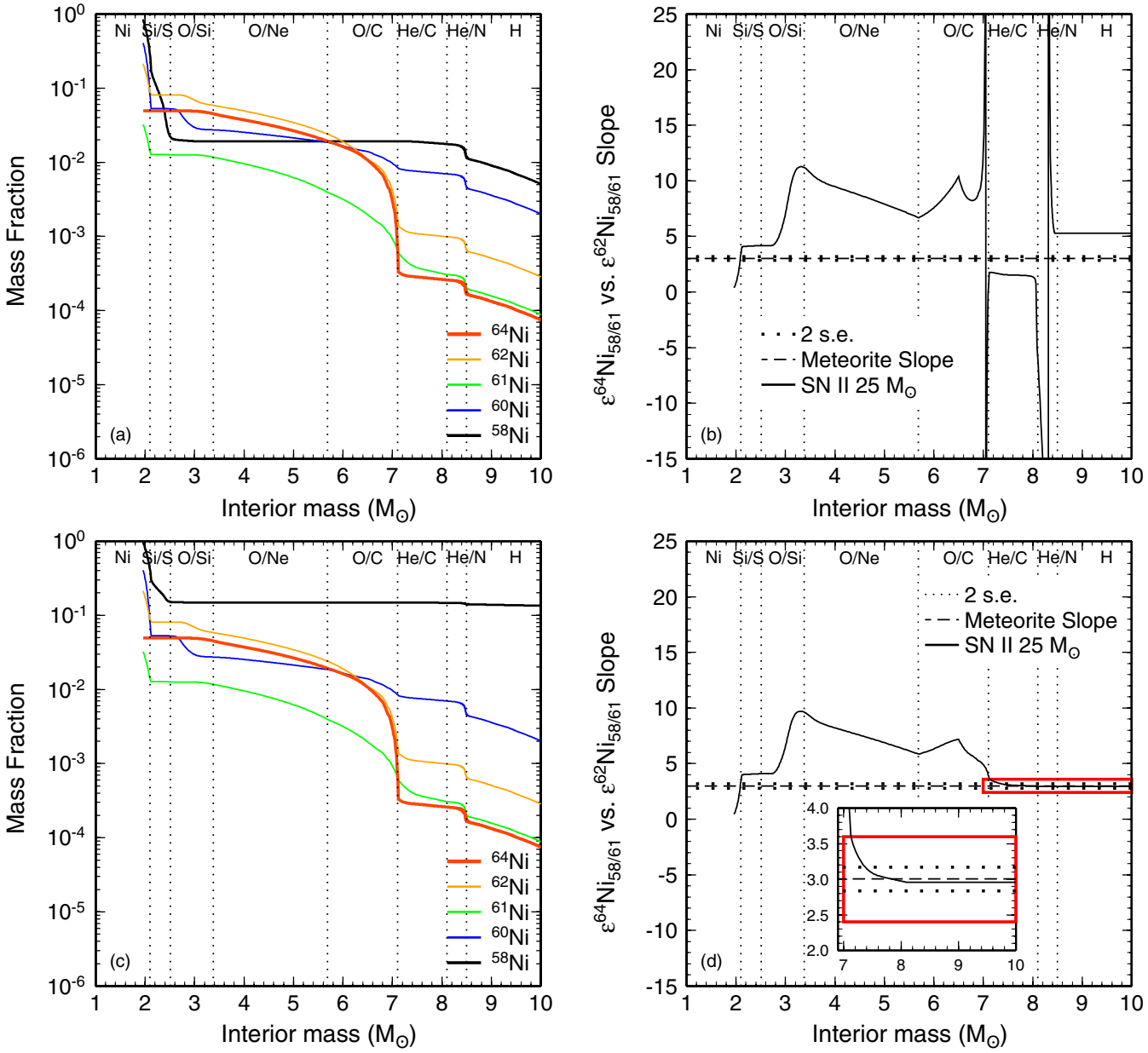

Figure 10. (a and b) The integrated shell yields from the outside of the supernova inward and the slope produced by mixing of these shells into the solar system. They show that neither the ^{58}Ni anomaly nor the correct slope are produced by these integrated compositions. (c and d) The same as (a and b) but in addition, mixing of the homogenized composition for the Si/S zone in to the integrated composition. They show that the Ni isotope signatures of the outer zones of the supernova (H, He/N, and He/C) may be dominated by that of the ^{58}Ni from the Si/S zone, while those of the middle zones (O/Si, O/Ne, and O/C) are not.

(A color version of this figure is available in the online journal.)

3.1.3. Combinations of Supernova Shells

Previous studies have often considered "mass cuts" of a supernova (see Rauscher et al. 2002, for a discussion of mass-cut location in these models): the averaged composition of material beyond a critical radius that is believed to be ejected rather than collapse onto the remnant core. We can also calculate the Ni isotope compositions of SN II ejecta for various mass cuts to investigate if the Ni isotope anomalies observed in the solar system can be provided by a single mass cut. The results of this are shown in Figures 10(a) and (b), which show that a single mass cut cannot provide the correct slope or the ^{58}Ni anomaly.

An important finding from pre-solar grains, believed to be delivered from supernovae (the so-called X-grains), is that their compositions reflect contributions of different elements from different zones of SN II events (e.g., Zinner 1998, 2003; Hammer et al. 2010). For example, Zinner (1998, 2003) suggested that pre-solar silicon carbide X-grains found in meteorites required input from the Ni and Si/S zones to account for large excesses of ^{28}Si and ^{44}Ca together with material from the He/C zone to provide the carbon. Hoppe et al. (2010) suggested that molecule formation before mixing and grain formation can help account for the intimate association of such contrasting isotopic signatures. Recent work by Marhas et al. (2008) documents the Ni and Fe isotope compositions of X-grains and infers that they are most compatible with nucleosynthesis in the He/N and He/C zones, which again contrasts with the ^{28}Si excesses of the SiC hosts. These observations show that specific phases can carry distinctive isotopic signatures from different parts of a supernova. Although the SiC X-grains

identified are not themselves an appropriate component to account for the solar system variability of Ni, other phases may specifically sample Ni from a zone that does fulfill the isotopic requirements.

The suggestion that anomalies observed in meteorites may be created by mixing between inner zones and outer zones of supernovae is supported by both astrophysical observations and dynamical modeling. An observational example comes from SN 1987A, the most extensively studied supernova to date, an SN II of a star with a main-sequence mass in the range 16–22 $M_{\odot}$ (Arnett et al. 1989). Based on the evolution of the light curves of iron group elements in SN 1987A, Spyromilio et al. (1990) and Li et al. (1993) concluded that these elements were concentrated in high-velocity "bullets" emanating from the core of the supernova. Dynamical modeling of such explosions show that "fingers" of material from deep within the supernova reach out and separate to form clumps that travel through the outer zones (Hammer et al. 2010). Kifonidis et al. (2003) produced two-dimensional simulations of core-collapse supernovae which showed that the He-rich zones slow and capture the clumps from the interior. However, in the three-dimensional simulations of Hammer et al. (2010), the clumps of "bullets" from the inner zones (Ni, Si/S) travel faster and overtake those of the middle O-rich zones, with the fastest penetrating deep into the outermost H zone.

We have examined the isotopic consequences of this mechanism by mixing homogenized compositions of "bullets" from the inner zones into the outer zones. To produce the component of Ni isotope heterogeneity evident in bulk solar system objects requires the mass cut to occur at the base of the Si/S zone. This is because the Ni zone contains significant amounts of stable Ni isotopes which perturb the signature ^{58}Ni of the Si/S zone. As discussed by Rauscher et al. (2002), the location of the mass cut is a point of some uncertainty and it may be justified to locate it at the base of the Si/S zone. Another possibility is that the "bullets" from the Ni zone have so much energy that they are not captured by the H zone and are lost to space (e.g., Burrows et al. 1995). Regardless of the mechanism, from its Ni abundance and isotope composition, it is clear that the material from the Ni zone is not heterogeneously sampled by bulk meteorites. So by taking just the innermost "bullets" from above the mass cut, which originate in the Si/S zone, and mixing these into the outer regions of the star, it is possible to examine the conditions under which the Ni isotope signature of the Si/S zone will survive.

Taking a bulk, homogenized composition from the Si/S zone and mixing it progressively with the rest of the supernova from the outside–in, the Si/S contribution dominates the averaged Ni isotopic composition after mixing with the H, He/N, and He/C zones, but addition of material from the O-rich zones significantly perturbs this averaged signature, see Figures 10(c) and (d). This is interesting because the models for the production of X-grains also requires these O-rich zones to be largely bypassed because they would produce an environment too oxidizing for SiC grains to form or for existing grains to survive (Ebel & Grossman 2001).

However, taking the entire Si/S zone and mixing it into the entire outer zones may not be the most realistic scenario, even in these one-dimensional models. A more realistic and interesting test is to examine the lower limit of Si/S zone mixing that produces appropriate Ni isotopic signatures. Mixing as little as 0.5% of the homogenized Si/S zone into the outer regions of the supernova, down to the base He/N zone, produces an average Ni isotope composition appropriate for the anomalous solar system component, see Figure 10(d). In the Crab Nebula, the expanding supernova remnant formed clumps in the outer shells (Hester 2008), which would have resulted in reducing the mass of the outer shells to which the Si/S zone was mixed. In summary, the Ni isotope signature from the central regions (the Si/S zone) is relatively resistant to dilution and the mechanism for its excavation is supported by astronomical observations and astrophysical modeling. Therefore, we propose that the Ni isotope signature observed in meteorites is compatible with variable input of material produced near the base of an SN II.

3.2. Neutron-poor Anomalies in Other Iron Group Elements

Previous studies of iron peak elements in CAIs (Lee et al. 1978; Jungck et al. 1984; Heydegger et al. 1979; Niemeyer & Lugmair 1980; Niederer et al. 1980; Birck & Lugmair 1988) and bulk meteorites (Rotaru et al. 1992; Trinquier et al. 2008, 2009) have suggested a component enriched in neutron-rich nuclides (^{48}Ca, ^{50}Ti, ^{54}Cr) which apparently contrasts with the findings of this study. Thus, we need to consider the implications of this previous work for our inferences.

The history of neutron-rich anomalies can be traced back to early observations of Ca. Significantly, the solar system as a whole has anomalously abundant ^{48}Ca relative to ^{46}Ca. In either slow or rapid neutron addition processes, both ^{48}Ca and ^{46}Ca should be made in at least comparable abundances. Strikingly, an excess and deficit of a ^{48}Ca-rich component (without significant variation in ^{46}Ca or other isotopes of Ca) was observed in two so-called fractionated, with unknown nuclear effects (FUN), CAIs EK1-4-1 and C1, respectively (Lee et al. 1978). These isotopic observations thus led to models which created ^{48}Ca anomalies through neutron-rich NSE (Hartmann et al. 1985; Meyer et al. 1996). Neutron-rich nuclear statistical equilibrium (NSE) can also produce other neutron-rich nuclides, although the full range of solar system abundances can only be recreated by mixing material produced over a range of different conditions, the multi-zone mixing process of Hartmann et al. (1985).

Given more recent high-precision isotopic measurements of bulk meteorites, it is now clear that the FUN CAIs do not carry the right isotopic signature to explain the large-scale, mass-independent isotopic variability in the solar system. For example, the Ti isotopic anomalies of the FUN inclusions reported by Niederer et al. (1985) do not correspond to those observed in bulk chondrites by Trinquier et al. (2009). The evidence for Ca anomalies solely on ^{48}Ca in normal CAIs is more equivocal as the literature on normal CAIs show a divergence in results, see Figure 11. Niederer & Papanastassiou (1984) found only hints of anomalies, whereas Jungck et al. (1984) found clear ^{48}Ca anomalies with all other isotope ratios being normal (albeit with $\pm$ 50 ‰ errors on ^{46}Ca). However, more recently, Moynier et al. (2010) have found $\varepsilon^{40}Ca_{42/44}$ anomalies, unrelated to radioactive decay, in addition to $\varepsilon^{48}Ca_{42/44}$ anomalies. This more recent work suggests that Ca may have both neutron-rich and neutron-poor anomalies and implies that the history of anomalous Ca may be more complex than simply variable input of ^{48}Ca.

There are undoubtedly anomalies on the neutron-rich ^{50}Ti, as determined in normal CAIs and bulk rock samples by double spiking (Niederer et al. 1985). However, as discussed earlier, the variability in the Ti isotopic signature of bulk solar system material can be produced in the O/Ne zone and neutron-rich NSE need not be invoked. The case for Cr is interesting as internally normalized, mass-independent Cr isotope ratios are traditionally expressed as ^{54}Cr anomalies, normalizing to

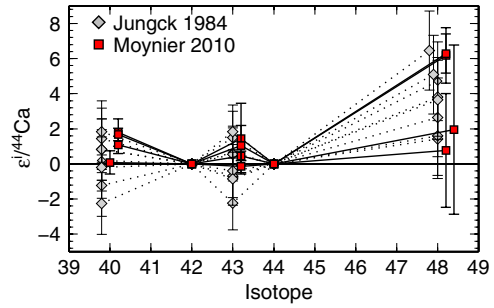

Figure 11. Internally normalized Ca isotope ratios from Jungck et al. (1984) and Moynier et al. (2010). The more precise data determined by Moynier et al. (2010) show anomalies in $\varepsilon^{40}Ca_{42/44}$ that could not be observed by Jungck et al. (1984). The data from Jungck et al. (1984) have been re-normalized to $\varepsilon^{i}Ca_{42/44}$. Due to their large uncertainties, $\varepsilon^{46}Ca_{42/44}$ have been omitted. Only data for high-precision total dissolutions of whole rocks and CAIs have been plotted.

(A color version of this figure is available in the online journal.)

$^{50}Cr/^{52}Cr$, but it must be noted that an anomaly in ^{54}Cr is equivalent to an anomaly in ^{50}Cr. We suggest that the inference of ^{54}Cr anomalies may have stemmed from the prior discovery of neutron-rich nuclides in Ti and Ca. To date, no absolute Cr isotope ratios have been published. However, by combining data from Trinquier et al. (2007, 2008) with the recent mass-dependent isotopic determinations of Moynier et al. (2011b) an approximation can be made, see Figure 12. While not ideal, as the mass-dependent and mass-independent compositions were determined during different studies, they give the best available opportunity to investigate the possibility of ^{50}Cr anomalies. From this combination of data, it is apparent that the CI chondrites, which have the largest ^{54}Cr mass-independent anomaly, are also most enriched in ^{50}Cr suggesting at least some component of the variation in Cr isotope anomalies may be in ^{50}Cr.

On the other hand, Dauphas et al. (2010) and Qin et al. (2011) have recently identified pre-solar grains with large ^{54}Cr excess. Nevertheless, there have been many pre-solar grains identified with highly anomalous Ti compositions (e.g., Ireland 1990; Alexander & Nittler 1999; Zinner 1998, 2003; Hoppe et al. 2010) yet variable proportions of the grains so far identified cannot account for the variations in bulk meteorites. In fact, there is a hint that the pre-solar compositions measured by Ireland (1990) in hibonites could be a candidate for the carrier of Ti isotope anomalies, but it remains that the majority of pre-solar grains so far identified do not play a significant role in the bulk meteorite variation. Moreover, as with Ti, a neutron-rich Cr composition does not require NSE and can be readily produced in an SN II (Qin et al. 2011).

In summary, we question the evidence for the dominant role of a component produced by neutron-rich NSE in causing the mass-independent variability of bulk meteorite samples and normal CAIs. We suggest that the casting of some iron peak mass-independent ratios as neutron-rich anomalies may more reflect the paradigm set by earlier work on FUN inclusions than a necessary implication of the data.

3.3. Processing in the Early Solar System: Incomplete Homogenization or Unmixing?

Input from the component from an SN II as identified above is heterogeneously distributed within the solar system, see Figures 1 and 5. Different meteorite groups are thought to have formed in different regions of the early solar system; they span a large range of heliocentric distances from the ECs closer to

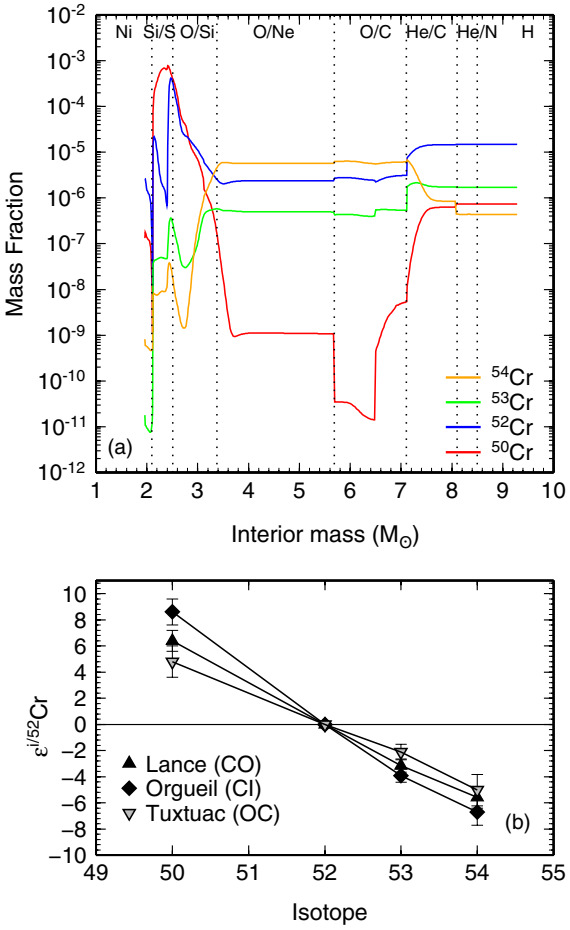

Figure 12. (a) Production of Cr isotopes through a 25 $M_\odot$ SN II. Data from Rauscher et al. (2002). (b) Absolute Cr isotope ratios estimated by combining mass-dependent fractionation taken from the $^{50}Cr/^{52}Cr$ of Moynier et al. (2011b) and the mass-independent data from Trinquier et al. (2007, 2008). As no absolute Cr isotope ratios have yet been published, these estimates give the best available indication of the location of Cr isotope anomalies. Orgueil and Lance were processed using data specific to each meteorite from both studies, however, Tuxtuac was only measured by Moynier et al. (2011b) so average OC compositions were used from Trinquier et al. (2007).

(A color version of this figure is available in the online journal.)

the Sun at <1 AU to the CCs further from the Sun at up to 4 AU (e.g., Wood 2005; Andreasen & Sharma 2007; Ciesla 2008). Thus, the range of Ni isotope anomalies between different meteorite groups, shown in Figure 1, is evidence for Ni isotope heterogeneity on a large scale in the early solar system.

It has previously been suggested that such large-scale isotope heterogeneity is due either to incomplete mixing of an anomalous component (e.g., Lee et al. 1979), or unmixing of previously homogeneously distributed components (e.g., Trinquier et al. 2009).

An important additional consideration for any model of solar system heterogeneity is that the magnitude, or indeed presence, of mass-independent isotopic variability in bulk samples is quite contrasting in elements influenced by similar nucleosynthetic processes. Thus, for iron group elements, large bulk isotopic anomalies have been identified in Ti and Cr (e.g., Leya et al. 2008; Trinquier et al. 2009; Trinquier et al. 2007), smaller variations are observed in Ni (e.g., Dauphas et al. 2008; Regelous et al. 2008; Steele et al. 2011), but no anomalies have yet been documented in bulk samples for Fe or Zn (Dauphas et al. 2008; Moynier et al. 2009). Similarly, there are striking

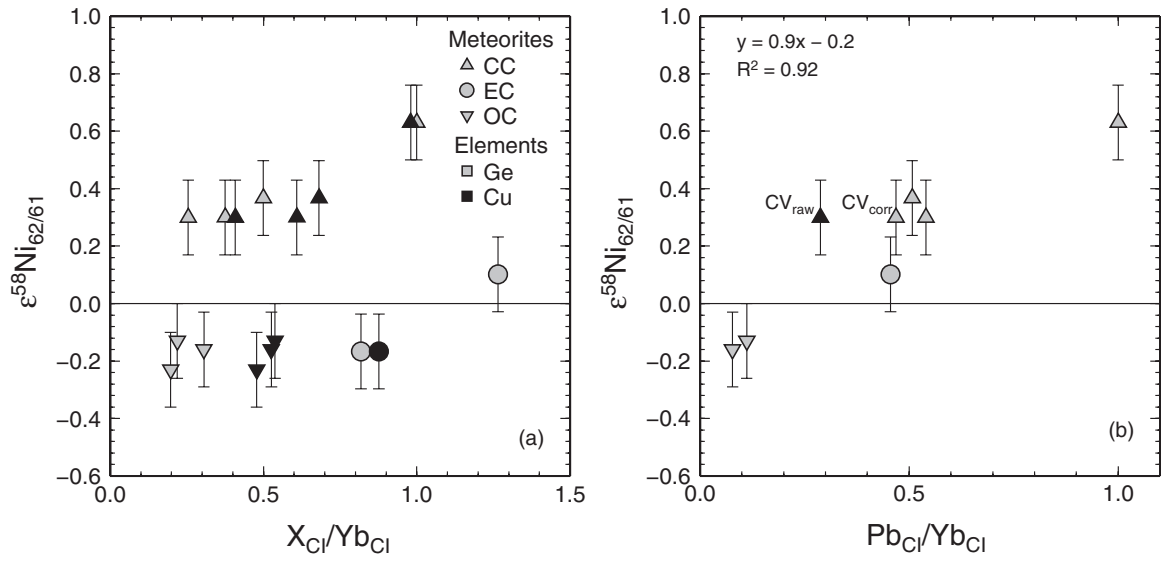

Figure 13. Plots showing the correlation between $\varepsilon^{58}Ni_{62/61}$ and elemental ratios in bulk chondrites. (a) The single monotonic correlation observed by Trinquier et al. (2009) between $\varepsilon^{54}Cr_{52/50}$ and Ge_{CI}/Yb_{CI} and Cu_{CI}/Yb_{CI} in the matrices of CCs form two correlations when the data are extended through the OCs and ECs. (b) A single monotonic correlation does exist between $\varepsilon^{58}Ni_{62/61}$ and Pb_{CI}/Yb_{CI}. CV_{raw} is the raw abundances ratio Pb/Yb in CV chondrites, whereas CV_{corr} is that with the CAI component removed. CV CCs contain significant proportions of CAIs which perturb the refractory element concentrations (e.g., Yb). This should not be as significant a consideration for other chondrite groups as they do not contain such high proportions of CAIs. Proportions and compositions for this correction from Grossman & Ganapathy (1976b), Grossman & Ganapathy (1976a), McSween (1977), and Grossman et al. (1979).

differences in the bulk, mass-independent isotopic compositions of Mo (Dauphas et al. 2002a), but barely perceptible anomalies in the neighboring Zr (Schönbächler et al. 2002; Akram et al. 2011) and none in the nucleosynthetically similar Os (Yokoyama et al. 2007). Yet sequential leaches of the primitive meteorites yield marked differences in mass-independent Zr and Os isotope ratios (Schönbächler et al. 2005; Yokoyama et al. 2010), as is also the case for Mo (Dauphas et al. 2002b). While exotic material seems widely present, as is also evident in the record of pre-solar grains, it is not always distributed evenly between different meteorite groups. We suggest that the different physical properties of the mineralogical hosts of isotopic anomalies of different elements may result in variable susceptibility to sorting processes in the solar nebula. This means that it may be important to consider not only the isotopic anomalies produced by mixing from a particular supernova zone, but also the phase in which elements of interest condense. For example, we noted that Ni but not Ti isotopic variations in bulk meteorites can be generated by a component from the Si/S zone. If Ni and Ti from the Si/S zone condense into different phases, we can invoke that the Ni-bearing phase was sorted in the early solar nebula, but the Ti-bearing phase from this zone remained homogeneously distributed. The converse would be true of material from the O/Ne zone. We would likewise argue that the host phases of the ^{96}Zr and ^{186}Os isotope anomalies did not suffer differential sorting in the nebula.

Possible supporting evidence that processing within the solar system resulted in the sorting of anomalous components was found by Trinquier et al. (2009) who noted that variations in $\varepsilon^{54}Cr_{52/50}$ were correlated with the abundance of moderately volatile elements to refractory elements in the matrices of CC. These elemental ratios are thought to be indices of volatile depletion—processing which occurred to varying extents at different heliocentric distances in the solar system (e.g., Wasson & Chou 1974; Bland et al. 2005). Trinquier et al. (2009) suggested that these correlations are indicative of preferential removal of previously well-mixed amorphous silicates which contained $\varepsilon^{54}Cr_{52/50}$ anomalies. This scenario was particularly favored by the authors because the neutron-rich ^{50}Ti anomaly was not thought to be produced in the same environment as the neutron-poor ^{46}Ti anomaly. By unmixing previously homogeneously distributed anomalies during processing within the solar system, the authors could reconcile correlated anomalies from different nucleosynthetic environments. We have shown that by considering effects on all Ti isotopes, including the normalizing isotopes, the anomalies observed in meteorites can be produced by one SN II event, which may mean processing within the solar system is not necessary to explain the correlation of $\varepsilon^{46}Ti_{49/47}$ versus $\varepsilon^{50}Ti_{49/47}$ but may be necessary for correlation with other elements.

Trinquier et al. (2009) only plotted a correlation between Ge/Yb and Cu/Yb in CCs, using chemical data from Bland et al. (2005). To extend these correlations to other chondrite groups, we have used equivalent data for bulk chondrites from Wasson & Kallemeyn (1988) and Kallemeyn et al. (1994). The correlations with Cu/Yb and Ge/Yb against $\varepsilon^{58}Ni_{62/61}$ are shown in Figure 13(a). These correlations are not continuous through all the chondrite groups; they in fact form two correlations, one comprising the CCs and the other OCs and ECs.

For the relative abundance of the more volatile element Pb, however, there is a single continuous correlation with ^{58}Ni. These observations have some resonance with the co-variations of the Ni isotopes themselves. Notably, $\varepsilon^{62}Ni_{58/61}$ and $\varepsilon^{64}Ni_{58/61}$ co-vary through all the chondrite groups, whereas in a plot of $\varepsilon^{60}Ni_{58/61}$ versus $\varepsilon^{62}Ni_{58/61}$, the CC and OC/EC form two different arrays. We would attribute this to $\varepsilon^{60}Ni_{58/61}$ anomalies being carried by a phase with different physical properties to that of the ^{58}Ni host. Indeed, the sulphide phases with large $\varepsilon^{60}Ni_{58/61}$ excesses identified by Tachibana & Huss (2003) could be a suitable candidate. Regardless of the details, the observations in Figures 3 and 13 indicate that the production of isotopic variation requires something more complex than a single mechanism such as thermal processing.

There are several interesting mechanisms by which radial grain size sorting may result from interaction between material in the disk and radiation from the protostar, namely, photophoresis, radiation pressure, and Poynting–Robertson drag. Some combination of these processes may account for the range of observations noted above. Photophoresis is the force exerted on an illuminated particle in a gas-rich environment due to differential temperatures of evaporation of gas molecules on the illuminated versus non-illuminated side; molecules on the illuminated side will evaporate with higher temperatures, and so velocities, causing greater momentum transfer (Krauss & Wurm 2005; Wurm et al. 2010).

Radiation pressure is the force exerted on an object being exposed to electromagnetic radiation from the Sun by transfer of momentum from solar photons (Burns et al. 1979). Poynting–Roberston drag is momentum loss that occurs due to re-radiation of energy from a moving particle (Robertson 1937; Burns et al. 1979). Burns et al. (1979) find that over a relatively narrow size range, 0.02–2 μm, for particles composed of iron, magnetite, and graphite, radiation pressure exceeds gravity as the dominant force, while at larger and smaller sizes or less metalloid compositions, Poynting–Roberston drag and gravity are more significant. These effects could clearly be significant in redistributing isotopically anomalous supernova grains with high metal content, while other grains may be the wrong size or composition. These mechanisms might explain why some elements are heterogeneously distributed and others are homogenous.

3.4. Live ^{60}Fe and Variation in $\varepsilon^{60}Ni_{58/61}$

Iron-60 decays to ^{60}Ni with a half-life of 2.62 ± 0.04 Ma (Rugel et al. 2009) and is of interest as an early solar system chronometer and a heat source for planetesimal melting. Studies of chondritic components by secondary ion mass spectrometry have suggested that there may have been a significant level of live ^{60}Fe in the early solar system up to 5×10^{-6} in ^{60}Fe/^{56}Fe$_0$ (Tachibana et al. 2006; Guan et al. 2007; Tachibana et al. 2007). However, recent high-precision studies of chemically purified mineral separates from differentiated achondrites and CB CCs show that the level of live ^{60}Fe must have been significantly lower, in the range 3×10^{-9}–2×10^{-8} (Quitté et al. 2010; Quitté et al. 2011; Moynier et al. 2011a).

A somewhat crude test of the level of live ^{60}Fe can be obtained from our bulk data set. Chondrites all have roughly the same Fe/Ni (16.5–18.1), therefore, they cannot distinguish between the effects of live or fossil ^{60}Fe, but iron meteorites have a large range of Fe/Ni, 4.8–16.7 (Regelous et al. 2008). Chondrite groups can be linked with iron meteorite groups based on similar nucleosynthetic isotope anomalies (e.g., $\varepsilon^{62}Ni_{58/61}$). This was suggested by Regelous et al. (2008) and is based on the assumption that meteorites with similar nucleosynthetic anomalies are derived from similar precursor material, and so would have received similar budgets of various components, for example, the carrier of extant or extinct ^{60}Fe and the source of stable isotope heterogeneity. Therefore, the ranges of Fe/Ni in iron meteorites can be used to make a prediction of the deficits in $\varepsilon^{60}Ni_{58/61}$ that should be present if live ^{60}Fe was present at the time of their formation. By comparing these with the observed deficits, it is possible to determine the maximum allowable ^{60}Fe/^{56}Fe$_0$. In our new data set, we have better defined the links between some chondrite-iron meteorite groups: CV and CO CCs are coupled with the IVB irons and the OCs are coupled with the IIAB, IIIAB, and IVA iron groups. Our higher-precision also makes it worthwhile revisiting the approach of Regelous et al. (2008) to place constraints on ^{60}Fe/^{56}Fe$_0$.

The largest difference in Fe/Ni ratios is between the group IVB irons (Fe/Ni 4.8) and the CV and CO chondrites (Fe/Ni ∼ 17). Assuming an initial ^{60}Fe/^{56}Fe$_0$ of 1×10^{-6} (e.g., Tachibana et al. 2006; Guan et al. 2007) a significant deficit of 0.35 ‰ would be expected for the IVB irons if they differentiated from a CO- or CV-like parent body, which would have appropriate $\varepsilon^{62}Ni_{58/61}$. From Figure 3 this clearly is not present. The weighted mean in $\varepsilon^{60}Ni_{58/61}$ of the CV/CO CCs is −0.096 ‰ ± 0.018 ‰, while the weighted mean of the IVB irons is −0.126 ‰ ± 0.009 ‰. This implies a ^{60}Fe/^{56}Fe$_0$ of 7.5×10^{-8} with a maximum of 1.4×10^{-7}. Thus, our bulk data are in agreement with the findings of Quitté et al. (2010). Quitté et al. (2011) and Moynier et al. (2011a) find that the level of live ^{60}Fe in the material from which the chondrites and irons formed was lower than previously thought. This low level of ^{60}Fe is compatible with the finding of neutron-poor mass-independent stable isotope anomalies and the suggestion that it results from an SN II. Iron-60 is the most neutron-rich Fe isotope with a long half-life; it is the equivalent to ^{64}Ni in the Ni system. A likely scenario for the origin of stable isotope heterogeneity in the early solar system is that it represents input of the last source to be added. If the nucleosynthetic source were neutron-rich NSE in an SN Ia, for example, then the level of ^{60}Fe would be significantly above the galactic background.

4. SUMMARY AND CONCLUSIONS

Nickel isotopic compositions have been determined for a variety of chondrite groups and show a range of 0.15 ‰, 0.29 ‰, and 0.84 ‰, in $\varepsilon^{60}Ni_{58/61}$ $\varepsilon^{62}Ni_{58/61}$, and $\varepsilon^{64}Ni_{58/61}$, respectively. Interestingly, the EH ECs alone match the terrestrial Ni isotope composition. A strong correlation is observed between $\varepsilon^{62}Ni_{58/61}$ and $\varepsilon^{64}Ni_{58/61}$ with a slope of 3.003 ± 0.166, which is within error of the slope expected from anomalies in ^{58}Ni. This hypothesis is supported by measurements of the absolute Ni isotope ratio of two samples that span a wide range in $\varepsilon^{62}Ni_{58/61}$ and $\varepsilon^{64}Ni_{58/61}$, Orgueil and Butsura, which show well-resolved anomalies in ^{58}Ni and no resolvable mass-independent effects in either ^{62}Ni or ^{64}Ni. Therefore, based on these absolute ratios, it seems likely that Ni isotope anomalies reside on the neutron-poor isotope ^{58}Ni and not the neutron-rich isotopes ^{62}Ni and ^{64}Ni. In $\varepsilon^{62}Ni_{58/61}$ and $\varepsilon^{64}Ni_{58/61}$, as with other isotope system (e.g., $\varepsilon^{54}Cr_{52/50}$), the CCs show the largest positive anomalies, ECs show approximately terrestrial ratios, and OCs have negative anomalies. As previously reported by Regelous et al. (2008), there is no overall correlation between $\varepsilon^{60}Ni_{58/61}$ and $\varepsilon^{62}Ni_{58/61}$.

We have examined the effects of mixing small fractions of the average compositions of various nucleosynthetic environments (SN Ia, SN II, AGB, and Wolf–Rayet star) into the solar system. These results have been compared with the slope of the correlation observed in meteorite samples which describes the large-scale heterogeneity in the early solar system. Bulk addition of material from the nucleosynthetic environments investigated cannot reproduce the correct slope in $\varepsilon^{64}Ni_{58/61}$ versus $\varepsilon^{62}Ni_{58/61}$ isotope space by generating ^{58}Ni anomalies, except for one SN Ia model which cannot simultaneously account for the heterogeneity observed in Ti isotopes.

Investigation of individual shells of SN II provides a more promising source for the isotopic heterogeneity observed in Ni and possibly other iron group elements (Ti and Cr). The Si/S zone of all masses of SN II that have been modeled by

Rauscher et al. (2002) can produce the correct slope in $\varepsilon^{64}Ni_{58/61}$ versus $\varepsilon^{62}Ni_{58/61}$ isotope space by overproduction of ^{58}Ni. Importantly, the O/Ne zone can produce approximately the Ti isotope signature observed in the solar system, i.e., correlated $\varepsilon^{46}Ti_{49/47}$ and $\varepsilon^{50}Ti_{49/47}$ with no anomalies in $\varepsilon^{48}Ti_{49/47}$. This is an important observation as previously it was thought this signature required multiple nucleosynthetic events (Trinquier et al. 2009). Moreover, the Ti isotope signature can be provided by the same nucleosynthetic event that can provide Ni isotope heterogeneity to the solar system. The Si/S zone overproduces ^{50}Cr relative to the other Cr isotopes, potentially implying that ^{50}Cr anomalies and not ^{54}Cr anomalies should exist in bulk meteorites. The hypothesis of neutron-poor isotope anomalies is supported by observations of anomalies in $\varepsilon^{40}Ca_{42/44}$ (Simon et al. 2009; Moynier et al. 2010). These observations are of particular significance because ^{40}Ca was used for normalization in early measurements on which the initial assumption of neutron-rich anomalies was based (Lee et al. 1978; Niederer & Papanastassiou 1984).

The specific mechanism by which inherited nucleosynthetic components are turned into mass-independent isotopic anomalies in bulk solar system materials remains unexplained. Two simple scenarios are possible: incomplete homogenization of anomalous material in the protosolar nebula and unmixing of anomalous material from a previously well-mixed molecular cloud during nebula formation and processing. The finding that some elements exhibit large anomalies in chondritic components, but none in the bulk, strongly suggests that an important control on the presence of isotopic anomalies is the susceptibility of carrier grains to solar system processing (e.g., Zr and Os; Schönbächler et al. 2003, 2005; Yokoyama et al. 2007; Yokoyama et al. 2010). Further evidence in support of this hypothesis is found from correlations between mass-independent Ni isotope anomalies and elemental ratios which presumably represent protosolar nebula processing. While continuous correlations between ratios of highly volatile elements over moderately refractory elements initially suggest sorting of volatile components, this is thought to be unlikely because carrier phases of such anomalies from meteorites to the solar system are thought to be refractory (Fedkin et al. 2010). Therefore, it may be more plausible that the correlations represent related differences in formation age or heliocentric distance of meteorite parent bodies. Some process that radially redistributes some isotopically anomalous grains relative to others could explain the variation of isotopic anomalies in most elements observed in meteorites. Three possible processes are photophoresis, radiation pressure, and Ponyting–Roberston drag, or some combination of the three, acting on grains differentially (Krauss & Wurm 2005; Wurm et al. 2010; Mukai & Yamamoto 1982; Jackson & Zook 1992; Burns et al. 1979). The lack of correlation of $\varepsilon^{60}Ni_{62/61}$ and $\varepsilon^{58}Ni_{62/61}$ anomalies is probably due to differential mixing of grains rich in fossil ^{60}Fe and grains with nucleosynthetic Ni isotope anomalies.

We are grateful to Derek Vance (BIG), Vyllinniskii Cameron (BIG), and Matthias Willbold (BIG) for advice and technical assistance, Sara Russell (NHM) and Caroline Smith (NHM) for helpful discussion and meteorite samples, and Andrew Davis (Chicago) for helpful discussion and providing AGB star data. We gratefully acknowledge an NERC studentship to RCJS (NE/F007329/1) and additional support from STFC (ST/F002734/1) and NHM that made this work possible. We thank the anonymous reviewer for their helpful comments which improved the manuscript and Frank Timmes for his editorial handling.

APPENDIX

A.1. Mass-independent Method

The chemical separation and mass spectrometric techniques used to acquire the data presented in this paper have been described in some detail in a previous study (Steele et al. 2011), but a brief summary below outlines the main features of the procedure. After dissolution using a standard HF–HNO_3 method, Ni was separated from terrestrial and meteorite samples using a four column ion-exchange procedure. The first column used the highly Ni specific reagent dimethylglyoxime (DMG), dissolved in a weak HCl–acetone solution, to elute Ni from a BioRad AG 50 column. This column separated Ni from the majority of the matrix and was performed twice. Subsequent columns reduced to the level of the blank acid the specific matrix components known to hinder Ni isotope analyses: Eichrom TRUspec to remove Fe which is an interference on ^{58}Ni, BioRad AG 50 to remove P and residual organics from breakdown of DMG and TRUspec, and BioRad AG MP 1 to reduce the ^{64}Zn interference on ^{64}Ni. The yield of the chemical separation procedure was determined to be within error of 100%.

The isotopic composition of Ni separated from meteorites by this method was then determined using a Neptune multiple-collector inductively coupled plasma mass spectrometer (MC-ICP-MS) in medium resolution ($M/\Delta M \geqslant 6000$) in order to resolve the minor molecular interferences present in the Ni mass range. Samples were introduced via a Cetac Aridus desolvating nebulizer, with a $\sim$50 μLmin^{-1} nebulizer tip. The interferences from ^{58}Fe on ^{58}Ni and ^{64}Zn on ^{64}Ni were reduced by effective chemical separation (see above) and corrected by peak stripping to a level where data accuracy was not affected. The Faraday cups collecting the ^{58}Ni and ^{60}Ni beams were connected to amplifiers fitted with 10^{10} Ω feedback resistors, allowing the precision limiting intensities of the minor isotopes to be increased to >40 pA while simultaneously collecting all isotopes. This high beam intensity on ^{64}Ni also helped minimize the influence of the Zn interference. Samples were analyzed at least four times in one analytical session, each analysis comprising 100 measurements of $\sim$8.4 s. On peak blank measurements bracketed every analysis of every sample or standard and were subtracted. Samples were internally normalized to a ^{58}Ni/^{61}Ni ratio of 59.722 (Gramlich et al. 1989a, 1989b) and are presented as ε units calculated relative to NIST SRM 986 (Gramlich et al. 1989a, 1989b) which was used as a bracketing standard for external normalization. These analyses yield typical precisions of 0.03 ‰, 0.05 ‰, and 0.08 ‰ (2 s.e. $n \geqslant 4$) for $\varepsilon^{60}Ni_{58/61}$, $\varepsilon^{62}Ni_{58/61}$, and $\varepsilon^{64}Ni_{58/61}$, where $\varepsilon^{i}Ni_{k/j}$ is the parts per ten thousand difference from a standard of the ratio i/j internally normalized to k/j, in this case ^{58}Ni/^{61}Ni. This precision is comparable to the reproducibility of multiple dissolutions of the same sample.

A.2. York Regression of Meteorite Samples

York regressions (York et al. 2004) on $\varepsilon^{64}Ni_{58/61}$ versus $\varepsilon^{62}Ni_{58/61}$ for the 30 meteorite and peridotite samples (spallation-affected Tlacotepec was omitted) were performed in three different ways as follows: (1) using the 215 individual analyses for which all five isotopes were measured, Table 3

Table 3
The First 10 Examples of the 215 Analyses for Which All Five Isotopes Were Measured

Sample	$\varepsilon^{62}Ni_{58/61}$	1 s.d.	$\varepsilon^{64}Ni_{58/61}$	1 s.d.
JP-1_004	0.068	0.042	0.106	0.082
JP-1_016	0.017	0.042	0.120	0.082
JP-1_028	0.028	0.042	0.084	0.082
JP-1_040	−0.002	0.042	0.141	0.082
JP-1_004	0.047	0.042	0.193	0.082
JP-1_008	0.019	0.042	0.121	0.082
JP-1_012	0.017	0.042	0.148	0.082
JP-1_016	0.026	0.042	0.055	0.082
JP-1_020	0.040	0.042	0.088	0.082
JP-1_004	0.050	0.042	0.131	0.082

Notes. The correlation coefficient between the errors in $\varepsilon^{62}Ni_{58/61}$ and $\varepsilon^{64}Ni_{58/61}$ is 0.68.

(This table is available in its entirety in a machine-readable form in the online journal. A portion is shown here for guidance regarding its form and content.)

(given in full in the online supplementary data); (2) using the 30 sample means and their homoscedastic standard errors (h.s.e.) explained in more detail in Appendix A.2.1, but in essence uncertainties are obtained using all analyses of all samples rather than just those for individual samples (see also Steele et al. 2011); and (3) using the 30 sample means and their standard errors (s.e.; i.e., Table 1 (main text)). Table 4 summarizes the results of the regressions. Details of how the errors and error correlations were calculated for each regression are given in Appendices A.2.1–A.2.3.

From Table 4, we see that the slopes (a) and (b) are in excellent agreement and both have acceptable MSWDs. We choose to report (a) in the main text for simplicity, i.e., there are fewer steps to the data reduction and the method is easier to understand. Method (b), however, benefits from 8, 12, and 8 additional measurements of $\varepsilon^{62}Ni_{58/61}$ on samples Bristol, Santa Clara, and JP-1, respectively, which, because there are no accompanying $\varepsilon^{64}Ni_{58/61}$ data, cannot be included in (a).

Regression (c) gives a different slope, albeit within error, and an MSWD of 1.7 which suggest the data are not from populations whose means lie on a straight line. We argue that (b) is preferred over (c) because the assigned errors are more robust in the former and that the high MSWD of (c) is to be expected. Intuitively, this is plausible as one might anticipate that the standard error may give over- and underestimates of the true error purely by chance when the number of repeat analyses is small and, furthermore, that the *underestimates* may have a greater influence on both the slope and MSWD than the overestimates. This has been confirmed by a Monte Carlo simulation.

First, we tested our Monte Carlo simulation code using a data set taken from Albarède (1995, Table 5.23, p. 304). The same data were used by York (York et al. 2004, Table II, data set 4) to compare the slope and intercept errors of the regression algorithm to that given by the simulation. Our York regression implementation gave a slope error in agreement with York et al. (2004) to the six decimal places published and an intercept error of 0.012985 compared to 0.012981. The relative difference from the Monte Carlo simulated errors are 0.007% (slope) and 0.006% (intercept) in our simulation of 10^8 trials compared to 0.037% and 0.037%, respectively, given by York's simulation (York et al. 2004) using 10^7 trials.

Table 4
York Regression (York et al. 2004) of $\varepsilon^{64}Ni_{58/61}$ vs. $\varepsilon^{62}Ni_{58/61}$ for All Meteorite Samples, Except Tlacotepec, and the Two Peridotites JP-1 and DTS-2

	n_Y	Slope	Slope Error (2σ)	MSWD	Monte Carlo Simulated	
					Slope Error (2 s.d.)	MSWD
(a)	215	3.003	0.166	1.021		
(b)	30	2.982	0.177	1.341	0.179	1.009
(c)	30	2.824	0.133	1.832	0.229	1.459

Notes. n_Y is the number of data points used in the regression. (a) Individual analyses with errors of 0.042 and 0.082 (1σ) for $\varepsilon^{62}Ni_{58/61}$ and $\varepsilon^{64}Ni_{58/61}$, respectively, and error correlation 0.68; (b) sample means with homoscedastic standard errors; (c) sample means with standard errors. For (b) and (c), the correlation used is given by Equation (A8). The rightmost two columns give slope errors and MSWD for regressions (b) and (c) estimated from a Monte Carlo simulation. See the Appendix (main text) for further details.

The Monte Carlo simulation of regression (c) is carried out as follows.

1. The York regression through the measured data is calculated to yield the least-squares adjusted data points or expectation values, see York et al. (2004).
2. Taking the expectation values in (1) as population means for each sample and using standard deviations of 0.042 and 0.082 for $\varepsilon^{62}Ni_{58/61}$ and $\varepsilon^{64}Ni_{58/61}$, respectively, and a correlation of 0.68 from the measured data, simulated data are generated. The number of simulated $\varepsilon^{62}Ni_{58/61}$ and $\varepsilon^{64}Ni_{58/61}$ data equals that in the measured data set for each sample.
3. The means and standard errors of each sample are calculated from the simulated data set, as is the correlation using Equation (A8). Note that we re-calculated r_0 from the simulated data rather than taking a value of 0.68.
4. York regression is performed using the means, standard errors, and correlations from (3). The slope, intercept, and MSWD are stored.
5. Steps 2–4 are repeated 10^7 times.
6. The standard deviation of the slopes and mean value of the MSWD are calculated and reported in Table 4.

The Monte Carlo simulation of regression (b) is carried out similarly but with homoscedastic standard errors calculated at step (3) rather than standard errors. The results of these simulations are given in Table 4. Note that for regression (b) the standard deviation of the simulated slopes, 0.179, is in excellent agreement with the slope error from the regression, 0.177, but this is not so for regression (c). In addition, the simulation of regression (c) gives an MSWD of 1.46 compared to a value close to 1 for regression (b). Hence, a high MSWD is to be expected if standard errors are used for the regression where rather small numbers of repeat analyses are made.

A.2.1. Regression Using Homoscedastic Errors

A homoscedastic data set is one where the data are drawn from a number of parent populations which may have different population means but share the same population variance. This may occur in practice where, as in the present case, many samples are analyzed under essentially identical conditions. Let the j^{th} analyses of sample i be denoted as x_{ij}. Let there be n_{xi} analyses of each sample and a total of N samples. Furthermore, we consider the x_{ij} to be drawn from populations with variance

σ_x^2. We can utilize all these data to make an unbiased estimate, s_x^2, of this variance given by Kenney & Keeping (1951, p. 164)

$$s_x^2 = \frac{1}{k_x}\sum_{i=1}^{N}\sum_{j=1}^{n_{xi}}(x_{ij} - \bar{x}_i)^2, \tag{A1}$$

where the sample mean, $\bar{x}_i$, and the number of degrees of freedom, k_x, are given by

$$\bar{x}_i = \frac{1}{n_{xi}}\sum_{j=1}^{n_{xi}} x_{ij} \tag{A2}$$

and

$$k_x = \left(\sum_{i=1}^{N} n_{xi}\right) - N. \tag{A3}$$

Thus, the homoscedastic standard error on the sample mean is

$$\text{h.s.e.} = \frac{s_x}{\sqrt{n_{xi}}}. \tag{A4}$$

Let x and y refer to $\varepsilon^{62}\text{Ni}_{58/61}$ and $\varepsilon^{64}\text{Ni}_{58/61}$, respectively. We use the entire data set to calculate s_x^2 and s_y^2, rather than only those used in the regression, a total of 375 and 312 analyses for x and y, respectively, on 36 samples giving $s_x = 0.042$ and $s_y = 0.082$.

In an analogous way, the covariance of the errors, s_{xy}, and their correlation, r_0, are given by

$$s_{xy} = \frac{1}{k}\sum_{i=1}^{N}\sum_{j=1}^{n_i}(x_{ij} - \bar{x}_i)(y_{ij} - \bar{y}_i) \tag{A5}$$

and

$$r_0 = \frac{s_{xy}}{s_x s_y} \tag{A6}$$

where

$$k = \left(\sum_{i=1}^{N} n_i\right) - N. \tag{A7}$$

The sum over j from 1 to n_i in Equation (A5) includes only those analyses where both x and y are measured; in our case, a total of 312 analyses giving $r_0 = 0.68$.

The correlation, r_i, between the means, $\bar{x}_i$ and $\bar{y}_i$, for those samples where every analysis measured both x and y is simply $r_i = r_0$. However, in the case of samples JP-1, Bristol, and Santa Clara, some analyses measured x only. The correlation for these three samples, therefore, needs special treatment and is given by

$$r_i = r_0\left(\frac{n_{yi}}{n_{xi}}\right)^{1/2}. \tag{A8}$$

This can be shown as follows. Consider

$$f = au + bw, \tag{A9}$$

where a and b are constants. Propagating the errors (denoted by s suitably subscripted) in u and w into f gives,

$$s_f^2 = a^2 s_u^2 + b^2 s_w^2. \tag{A10}$$

Now, let v be correlated with u with covariance s_{uv}, but not with w. The covariance between f and v is given by

$$s_{fv} = \frac{\partial f}{\partial u} s_{uv} \tag{A11}$$

$$= a\, s_{uv}. \tag{A12}$$

Replacing the covariances with correlations, r_{fv} and r_{uv}, gives

$$r_{fv} = a\, r_{uv}\frac{s_u}{s_f} \tag{A13}$$

$$= r_{uv}\left(\frac{a^2 s_u^2}{a^2 s_u^2 + b^2 s_w^2}\right)^{1/2}, \tag{A14}$$

where we have substituted s_f from Equation (A10).

If we have n correlated measurements of x and y, giving means $\bar{x}_n$ and $\bar{y}$, and a further m measurements of x with mean $\bar{x}_m$ then $\bar{x}$, then the mean of all $n+m$ measurements of x is given by

$$(n+m)\bar{x} = n\bar{x}_n + m\bar{x}_m. \tag{A15}$$

Equation (A15) is identical to Equation (A9) with $f \to \bar{x}$, $u \to \bar{x}_n$, $w \to \bar{x}_m$, $a \to n/(n+m)$, and $b \to m/(n+m)$. Finally, by substituting $v \to \bar{y}$ and $r_{fv} \to r$, Equation (A14) becomes

$$r = r_{\bar{x}_n\bar{y}}\left(\frac{n^2 s_{\bar{x}_n}^2}{n^2 s_{\bar{x}_n}^2 + m^2 s_{\bar{x}_m}^2}\right)^{1/2}, \tag{A16}$$

where r is the correlation between the errors in $\bar{x}$ and $\bar{y}$. If the analyses are from a single population, then we can use $ns_{\bar{x}_n}^2 = ms_{\bar{x}_m}^2$ and Equation (A16) becomes

$$r = r_{\bar{x}_n\bar{y}}\left(\frac{n}{n+m}\right)^{1/2}. \tag{A17}$$

Lastly, in the homoscedastic case, we have $r_{\bar{x}_n\bar{y}} = r_0$ and putting $r \to r_i$, $n \to n_{yi}$, and $n+m \to n_{xi}$ completes the proof of Equation (A8). Table 5 shows the calculated values of r_i for each sample. Note that the values in columns "n" and "n_{64}" in Table 5 correspond to n_{xi} and n_{yi}, respectively.

A.2.2. Regression Using Individual Analyses

In this case, we are constrained to regress only using those analyses for which both $\varepsilon^{62}\text{Ni}_{58/61}$ (x) and $\varepsilon^{64}\text{Ni}_{58/61}$ (y) are measured. We assign errors $s_x = 0.042$ and $s_y = 0.082$, respectively, and correlation $r_0 = 0.68$, given by Equations (A1) and (A6), to each analysis.

A.2.3. Regression Using Standard Errors

This may be considered the more conventional approach where the error used for the regression is the standard error (s.e.) calculated on a sample by sample basis. The sample standard deviation, s_{xi}, and standard error are given by

$$s_{xi}^2 = \frac{1}{n_{xi} - 1}\sum_{j=1}^{n_{xi}}(x_{ij} - \bar{x}_i)^2 \tag{A18}$$

$$\text{s.e.} = \frac{s_{xi}}{\sqrt{n_{xi}}}. \tag{A19}$$

Table 5
Sample Means of $\varepsilon^{60}Ni_{58/61}$, $\varepsilon^{62}Ni_{58/61}$, and $\varepsilon^{64}Ni_{58/61}$ Taken from Table 1 (Main Text) and from Steele et al. (2011)

	Group	NHM No.	n	n_{64}	$\varepsilon^{60}Ni_{58/61}$	2 h.s.e.	$\varepsilon^{62}Ni_{58/61}$	2 h.s.e.	$\varepsilon^{64}Ni_{58/61}$	2 h.s.e.	r
Carbonaceous chondrites											
Orgueil	CI	1985, M148	4	4	−0.008	0.025	0.203	0.042	0.585	0.082	0.68
Cold Bokkeveld	CM	1919, 144	4	4	−0.084	0.025	0.113	0.042	0.335	0.082	0.68
Murchison	CM	...	4	4	−0.098	0.025	0.124	0.042	0.298	0.082	0.68
Felix	CO	...	4	4	−0.079	0.025	0.097	0.042	0.262	0.082	0.68
NWA 801	CR	1919, 89	5	5	−0.157	0.022	0.116	0.038	0.361	0.073	0.68
Allende	CV	1988, M23	4	4	−0.098	0.025	0.131	0.042	0.324	0.082	0.68
Leoville	CV	13989	8	8	−0.107	0.018	0.061	0.030	0.135	0.058	0.68
Enstatite chondrites											
Abee	EH	51366	4	4	−0.007	0.025	0.027	0.042	0.084	0.082	0.68
St. Mark's	EH	1990, 339	4	4	−0.017	0.025	0.039	0.042	0.113	0.082	0.68
Khairpur	EL	992, M7	4	4	−0.023	0.025	−0.054	0.042	−0.049	0.082	0.68
Ordinary chondrites											
Butsura	H	...	28	28	−0.048	0.009	−0.053	0.016	−0.171	0.031	0.68
Ceniceros	H	1915, 86	4	4	−0.063	0.025	−0.050	0.042	−0.078	0.082	0.68
Barratta	L	1975, M11	4	4	−0.042	0.025	−0.028	0.042	−0.105	0.082	0.68
Tenham	L	...	4	4	−0.026	0.025	−0.057	0.042	−0.117	0.082	0.68
Tieschitz	HL	...	8	8	−0.052	0.018	−0.080	0.030	−0.253	0.058	0.68
Chainpur	LL	...	8	8	−0.054	0.018	−0.065	0.030	−0.171	0.058	0.68
Dhurmsala	LL	...	4	4	−0.049	0.025	−0.085	0.042	−0.210	0.082	0.68
Iron meteorites											
Coahuila	2AB	54242	4	4	−0.031	0.025	−0.088	0.042	−0.259	0.082	0.68
Henbury	3AB	...	4	4	−0.056	0.025	−0.090	0.042	−0.304	0.082	0.68
Lenarto	3AB	61304	4	4	−0.047	0.025	−0.083	0.042	−0.318	0.082	0.68
Arispe	IC	86425	4	4	−0.049	0.025	−0.129	0.042	−0.317	0.082	0.68
Bendegó	IC	66585	4	4	−0.013	0.025	−0.001	0.042	−0.030	0.082	0.68
Bristol	IVA	1955226	16	8	−0.048	0.013	−0.047	0.021	−0.165	0.058	0.48
Putnam County	IVA	90228	8	8	−0.049	0.018	−0.069	0.030	−0.243	0.058	0.68
Skookum	IVB	...	4	4	−0.129	0.025	0.067	0.042	0.168	0.082	0.68
Cape of Good Hope	IVB	1985,M246	4	4	−0.126	0.025	0.099	0.042	0.271	0.082	0.68
Hoba	IVB	1930976	8	8	−0.122	0.018	0.084	0.030	0.214	0.058	0.68
Santa Clara	IVB	1983,M27	16	4	−0.121	0.013	0.087	0.021	0.369	0.082	0.34
Tlacotepec	IVB	1959913	4	4	−0.136	0.025	0.023	0.042	0.134	0.082	0.68
Terrestrial samples and standards											
PtYG	T	...	20	20	0.010	0.011	−0.009	0.019	0.012	0.037	0.68
NiSalt	T	...	16	16	−0.016	0.013	0.058	0.021	0.226	0.041	0.68
CPI	T	...	16	12	0.002	0.013	0.017	0.021	0.083	0.047	0.59
NIST SRM 986-Col	T	...	4	4	0.002	0.025	−0.024	0.042	0.000	0.082	0.68
DTS-2	T	...	4	4	−0.007	0.025	0.038	0.042	0.161	0.082	0.68
JP-1	T	...	58	50	−0.006	0.007	0.035	0.011	0.117	0.023	0.63
NIST SRM 361	T	...	72	41	−0.011	0.006	0.029	0.010	0.136	0.026	0.51

Note. 2 h.s.e. errors are two standard deviations of the mean based on an assumption of homoscedasticity for the set of individual analyses of all samples and standards analyzed during this study; see the text for details.

The correlation may be calculated similarly on a sample by sample basis, thus

$$r_i' = \frac{\sum_{j=1}^{n_i}(x_{ij} - \bar{x}_i)(y_{ij} - \bar{y}_i)}{\sqrt{\sum_{j=1}^{n_i}(x_{ij} - \bar{x}_i)^2 \sum_{j=1}^{n_i}(y_{ij} - \bar{y}_i)^2}}. \quad \text{(A20)}$$

However, for small sample sizes, typically $n_i = 4$ in the present case, r_i' is poorly constrained. This can be demonstrated by a Monte Carlo simulation of pseudorandom, normally distributed data pairs with a population correlation $\rho = 0.68$. For $n = 4$, the 95% lower and upper confidence limits on r_i' are −0.66 and +0.99, respectively. With such wide confidence limits it may be of little value to include the correlation in the regression at all, so we prefer to use the more robust correlation calculated from the entire data set using Equation (A8) as we do for the homoscedastic case.

A.3. Mass-dependent Method to Obtain "Absolute" Ratios

Analysis by adding a double spike isotopic tracer (Dietz et al. 1962; Dodson 1963, 1969; Russell 1971) provides a robust method for obtaining the natural mass-dependent isotopic fractionation of elements with four or more isotopes. A ^{61}Ni–^{62}Ni double spike technique established in Bristol has been previously described by Cameron et al. (2009). However, the technique of Cameron et al. (2009) was set up to investigate the isotopic fractionations in a large number of samples where the highest precision was not a critical concern. By contrast, in the present study, we require high-precision measurements of a small number of samples. We have chosen two samples which span the largest range in $\varepsilon^{64}Ni_{58/61}$, Orgueil +0.585 and Butsura −0.160. To determine which isotopic abundances vary to produce this 0.75 ‰ difference requires a precision better than ∼0.40 ‰, whereas Cameron et al. (2009) report a precision

of 0.8 ‰. We have, therefore, adjusted the techniques slightly to re-optimize for higher precision at the expense of sample throughput. The changes are outlined below, along with a short discussion of the precision.

A.3.1. Double Spike Inversion

Double spike inversion for natural mass-dependent fractionation works by adding an isotopic tracer with two highly enriched isotopes to a sample. The ratio of these two isotopes can then be used as an internal standard to correct for instrumental mass fractionation, thus any residual fractionation that occurred prior to analysis (e.g., Dodson 1963; Russell 1971). In order to determine the absolute ratios requires the following to be known: (1) the composition of the double spike, (2) the mass fractionation curve which passes through the sample composition, and (3) the measured composition of the sample spike mixture. The mass fractionation curve is defined by the exponential (kinetic) mass fractionation law, assumed to be an accurate model of both the instrumental and natural isotopic fractionation, and one known composition lying on the curve, **n**. For samples with isotopic anomalies, as in the present case or for Pb isotopes (e.g., Compston & Oversby 1969), a separate internally normalized measurement of the unspiked sample defines **n**.

Samples were spiked in a ∼1:1 ratio with an ^{61}Ni:^{62}Ni spike in approximate molar proportions of 40% and 60% following Cameron et al. (2009). The four isotopes used for the inversion were ^{58}Ni, ^{60}Ni, ^{61}Ni, and ^{62}Ni.

Analyses were made on the second Thermo Finnigan Neptune multiple-collector inductively-coupled plasma mass spectrometer (MC-ICP-MS; serial No. 1020) in Bristol using an introduction system set up similar to the one used for the mass-independent analyses with the Cetac Aridus desolvating nebulizer, 50 μLmin^{-1} nebulizer tip, ∼10 mLmin^{-1} of N_2. However, the mass spectrometer was set up differently and used low resolution and a different cup configuration. Molecular interferences, e.g., ^{40}Ar^{18}O, were reduced to background levels by use of N_2 and were subtracted by on peak blank correction (see below).

The two samples chosen for double spike analysis (Orgueil and Butsura) were measured multiple times in one analytical session that followed approximately the same analytical protocol as Cameron et al. (2009). At the beginning of the sequence, and interleaved with spiked samples throughout the sequence, a number of unspiked NIST SRM 986 analyses were made which were used to correct for any non-exponential fractionation or other non-exponential effects, for example, Faraday cup yield factors. Spiked samples were measured in groups of between three and five analyses, which included: spiked NIST SRM 986 with mixture ratios of 0.5, 1, and 2; and Orgueil; and Butsura in mixture ratios of 1. Spiked meteorites were each analyzed eight times interleaved throughout the analytical session. Two washes were performed after each analysis to clean the spray chamber, and peak blanks were measured after each analysis. Spiked samples, where all isotopes have approximately the same abundance, were run at ∼200 pA for the most abundant isotope. Approximately 10 μg of sample Ni was consumed in total for each meteorite.

A.3.2. Mass-dependent Precision

The results of the eight repeat measurements of Orgueil and Butsura are given in Table 2 (main text), Table 6, and Figure 4. These analyses yield an uncertainty for the ^{58}Ni/^{61}Ni ratio of 0.15 ‰ – 0.2 ‰ 2 s.e. for the eight repeat measurements. The uncertainty in the absolute isotope ratios of samples, however, must include errors on both the mass-dependent and mass-independent measurements. This problem needs to be assessed with care as errors in any one isotope used in the double spike inversion can affect all the reported ratios. A more obvious problem is that we do not calculate an error for the ^{58}Ni/^{61}Ni ratio in the mass-independent data as it is the normalizing ratio. Thus, we undertook a simulation using a modeled composition with mass-dependent fractionation of zero. These data were processed through the double spike inversion with mass-independent anomalies for each ratio (i.e., ε^{60}Ni$_{58/61}$, ε^{62}Ni$_{58/61}$, and ε^{64}Ni$_{58/61}$) varied randomly around zero in a distribution with a standard deviation (s.d.) equal to that of the uncertainty on the mass-independent data (0.03 ‰, 0.05 ‰, and 0.08 ‰). We made 5000 inversions to build up a robust model of the uncertainty in the absolute ratios. The results of this simulation are given in Table 7. They show that the contribution to the uncertainty on the absolute ratio from the precision of the mass-independent data is significant relative to the precision of the mass-dependent, and therefore must be included in the uncertainty of the absolute ratios. The uncertainty contribution from the mass-independent measurements (as modeled above) and the uncertainty from the mass-dependent measurement have thus been summed in quadrature to obtain the overall precision of the absolute ratios quoted in Table 2 (main text).

The external reproducibility of analyses made by this technique has been assessed using measurements of NIST SRM 986, spiked in a 1:1 ratio made in seven analytical session over a 18 month period, kindly provided by Derek Vance and Vyllinniskii Cameron. These analyses yield an error with 2 standard deviations (2 s.d.) of 0.59 somewhat larger than the

Table 6
Absolute Ratios for Two Meteorites Which Cover a Large Range in ε^{64}Ni$_{58/61}$

	$\varepsilon^{58/61}$Ni	$\varepsilon^{60/61}$Ni	$\varepsilon^{61/61}$Ni	$\varepsilon^{62/61}$Ni	$\varepsilon^{64/61}$Ni
Butsura					
i	−3.05	−1.05	0.00	0.93	2.74
ii	−2.95	−1.02	0.00	0.90	2.64
iii	−2.81	−0.97	0.00	0.85	2.51
iv	−2.93	−1.01	0.00	0.89	2.62
v	−2.89	−1.00	0.00	0.88	2.58
vi	−3.02	−1.04	0.00	0.92	2.71
vii	−3.15	−1.08	0.00	0.96	2.83
viii	−3.19	−1.10	0.00	0.98	2.87
Average	−3.00	−1.03	0.00	0.91	2.69
2 s.e.	0.09	0.03	0.00	0.03	0.09
Orgueil					
i	−1.98	−0.66	0.00	0.84	2.47
ii	−2.59	−0.86	0.00	1.04	3.06
iii	−2.27	−0.75	0.00	0.94	2.75
iv	−2.12	−0.70	0.00	0.89	2.61
v	−1.92	−0.64	0.00	0.82	2.41
vi	−2.28	−0.76	0.00	0.94	2.76
vii	−2.11	−0.70	0.00	0.88	2.60
viii	−2.07	−0.69	0.00	0.87	2.56
Average	−2.17	−0.72	0.00	0.90	2.65
2 s.e.	0.15	0.05	0.00	0.05	0.14

Notes. These data show good evidence that these two samples, and by inference the data set as a whole, contain ^{58}Ni anomalies and not correlated ^{62}Ni and ^{64}Ni anomalies. The uncertainties include contributions from the mass-dependent analyses, mass-independent analyses, and the standards used for the second normalization.

Table 7
The Effect of Uncertainty on the Mass-independent Anomaly of Samples on the Double Spike Inversion. These Data Were Obtained Using Monte Carlo Simulation (Top). The Uncertainty Contribution from the Spiked Standards Used for Normalization and Measured During the Analytical Session (Bottom)

	$\varepsilon^{58/61}$Ni	$\varepsilon^{60/61}$Ni	$\varepsilon^{61/61}$Ni	$\varepsilon^{62/61}$Ni	$\varepsilon^{64/61}$Ni
Monte Carlo simulation of mass-independent contribution to uncertainty					
Average	0.00	0.00	0.00	0.00	0.00
2 s.d.	0.05	0.01	0.00	0.05	0.10
Contribution to uncertainty from 1:1 standard spike mixtures					
Average	−0.17	−0.06	0.00	0.05	0.16
2 s.e.	0.20	0.06	0.00	0.06	0.19

Notes. These data were obtained using Monte Carlo simulation. Bottom: The uncertainty contribution from the spiked standards used for normalization and measured during the analytical session.

2 s.d. of the meteorite data made in a single session (∼0.34 ‰). Thus, the contribution to the uncertainty on the absolute ratio from the mass-dependent measurements is more realistically greater by a factor of roughly two than that determined from the within run precision (2 s.e. = 0.21 ‰), but this is still sufficient to resolve the 0.75 ‰ difference between meteorites, see Section 2.1.

REFERENCES

Akram, W., Schonbachler, M., Williams, H., & Halliday, A. 2011, in Lunar and Planetary Institute Science Conference Abstracts, Vol. 42, The Origin of Nucleosynthetic Zirconium-96 Heterogeneities in the Inner Solar System, ed. S. J. Mackwell (Houston: LPI), 1908
Albarède, F. 1995, Introduction to Geochemical Modeling (Cambridge: Cambridge Univ. Press)
Alexander, C. M. O., & Nittler, L. R. 1999, ApJ, 519, 222
Andreasen, R., & Sharma, M. 2007, ApJ, 665, 874
Arnett, W. D., Bahcall, J. N., Kirshner, R. P., & Woosley, S. E. 1989, ARA&A, 27, 629
Birck, J. L., & Lugmair, G. W. 1988, Earth Planet. Sci. Lett., 90, 131
Bland, P., Alard, O., Benedix, G., et al. 2005, Proc. Natl. Acad. Sci., 102, 13755
Burbidge, E. M., Burbidge, G. R., Fowler, W. A., & Hoyle, F. 1957, Rev. Mod. Phys., 29, 547
Burns, J., Lamy, P., & Soter, S. 1979, Icarus, 40, 1
Burrows, A., Hayes, J., & Fryxell, B. 1995, ApJ, 450, 830
Cameron, V., Vance, D., Archer, C., & House, C. H. 2009, Proc. Natl. Acad. Sci., 106, 10944
Ciesla, F. 2008, Meteorit. Planet. Sci., 43, 639
Compston, W., & Oversby, V. 1969, J. Geophys. Res., 74, 4338
Dauphas, N., Cook, D. L., Sacarabany, A., et al. 2008, ApJ, 686, 560
Dauphas, N., Marty, B., & Reisberg, L. 2002a, ApJ, 565, 640
Dauphas, N., Marty, B., & Reisberg, L. 2002b, ApJ, 569, L139
Dauphas, N., Remusat, L., Chen, J. H., et al. 2010, ApJ, 720, 1577
Dietz, L. A., Paghugki, C. F., & Land, G. A. 1962, Anal. Chem., 34, 709
Dodson, M. 1963, J. Sci. Instrum., 40, 289
Dodson, M. H. 1969, J. Sci. Instrum., 2, 490
Ebel, D. S., & Grossman, L. 2001, Geochim. Cosmochim. Acta, 65, 469
Fedkin, A. V., Meyer, B. S., & Grossman, L. 2010, Geochim. Cosmochim. Acta, 74, 3642
Gramlich, J. W., Machlan, L. A., Barnes, I. L., & Paulsen, P. J. 1989a, J. Res. Natl. Inst. Stand. Technol., 94, 347
Gramlich, J. W., Machlan, L. A., Barnes, I. L., & Paulsen, P. J. 1989b, J. Res. Natl. Inst. Stand. Technol., 94, 357
Grossman, L., & Ganapathy, R. 1976a, Geochim. Cosmochim. Acta, 40, 331
Grossman, L., & Ganapathy, R. 1976b, Geochim. Cosmochim. Acta, 40, 967
Grossman, L., Ganapathy, R., Methot, R. L., & Davis, A. M. 1979, Geochim. Cosmochim. Acta, 43, 817
Guan, Y., Huss, G., & Leshin, L. 2007, Geochim. Cosmochim. Acta, 71, 4082
Hammer, N. J., Janka, H. T., & Müller, E. 2010, ApJ, 714, 1371
Hartmann, D., Woosley, S. E., & El Eid, M. F. 1985, ApJ, 297, 837
Hashimoto, M. 1995, Prog. Theor. Phys., 94, 663
Hester, J. 2008, ARA&A, 46, 127
Heydegger, H. R., Foster, J. J., & Compston, W. 1979, Nature, 278, 704
Hoppe, P., Leitner, J., Gröner, E., et al. 2010, ApJ, 719, 1370
Ireland, T. R. 1990, Geochim. Cosmochim. Acta, 54, 3219
Iwamoto, K., Brachwitz, F., Nomoto, K., et al. 1999, ApJS, 125, 439
Jackson, A. A., & Zook, H. A. 1992, Icarus, 97, 70
Jungck, M. H. A., Shimamura, T., & Lugmair, G. W. 1984, Geochim. Cosmochim. Acta, 48, 2651
Kallemeyn, G., Rubin, A., & Wasson, J. 1994, Geochim. Cosmochim. Acta, 58, 2873
Kasen, D., Röpke, F. K., & Woosley, S. E. 2009, Nature, 460, 869
Kenney, J., & Keeping, E. 1951, Mathematics of Statistics, Part Two (2nd ed.; Princeton, NJ: D. Van Nostrand Company, Inc.)
Kifonidis, K., Plewa, T., Janka, H.-T., & Müller, E. 2003, A&A, 408, 621
Krauss, O., & Wurm, G. 2005, ApJ, 630, 1088
Lee, T., Papanastassiou, D. A., & Wasserburg, G. J. 1978, ApJ, 220, L21
Lee, T., Russell, W. A., & Wasserburg, G. J. 1979, ApJ, 228, L93
Leya, I., Schönbächler, M., Krähenbühl, U., & Halliday, A. N. 2009, ApJ, 702, 1118
Leya, I., Schönbächler, M., Wiechert, U., Krähenbühl, U., & Halliday, A. N. 2008, Earth Planet. Sci. Lett., 266, 233
Li, H., McCray, R., & Sunyaev, R. A. 1993, ApJ, 419, 824
Liu, M.-C., McKeegan, K. D., Goswami, J. N., et al. 2009, Geochim. Cosmochim. Acta, 73, 5051
Lugaro, M., Davis, A. M., Gallino, R., Savina, M. R., & Pellin, M. J. 2004, Mem. Soc. Astron. Ital., 75, 723
Maeda, K., Röpke, F. K., Fink, M., et al. 2010, ApJ, 712, 624
Mahon, K. 1996, Int. Geol. Rev., 38, 293
Marhas, K., Amari, S., Gyngard, F., Zinner, E., & Gallino, R. 2008, ApJ, 689, 622
McSween, H. Y., Jr. 1977, Geochim. Cosmochim. Acta, 41, 1777
Meyer, B. S., Krishnan, T. D., & Clayton, D. D. 1996, ApJ, 462, 825
Meyer, B. S., Weaver, T. A., & Woosley, S. E. 1995, Meteoritics, 30, 325
Moynier, F., Blichert-Toft, J., Wang, K., Herzog, G. F., & Albarede, F. 2011a, ApJ, 741, 71
Moynier, F., Dauphas, N., & Podosek, F. A. 2009, ApJ, 700, L92
Moynier, F., Simon, J. I., Podosek, F. A., et al. 2010, ApJ, 718, L7
Moynier, F., Yin, Q.-Z., & Schauble, E. 2011b, Science, 331, 1417
Mukai, T., & Yamamoto, T. 1982, A&A, 107, 97
Niederer, F. R., & Papanastassiou, D. A. 1984, Geochim. Cosmochim. Acta, 48, 1279
Niederer, F. R., Papanastassiou, D. A., & Wasserburg, G. J. 1980, ApJ, 240, L73
Niederer, F. R., Papanastassiou, D. A., & Wasserburg, G. J. 1985, Geochim. Cosmochim. Acta, 49, 835
Niemeyer, S., & Lugmair, G. W. 1980, Meteoritics, 15, 341
Nomoto, K. 1982, ApJ, 253, 798
Nomoto, K., Hashimoto, M., Tsujimoto, T., et al. 1997, Nucl. Phys. A, 616, 79
Qin, L., Nittler, L. R., Alexander, C. M. O., et al. 2011, Geochim. Cosmochim. Acta, 75, 629
Quitté, G., Latkoczy, C., Schönbächler, M., Halliday, A. N., & Günther, D. 2011, Geochim. Cosmochim. Acta, 75, 7698
Quitté, G., Markowski, A., Latkoczy, C., Gabriel, A., & Pack, A. 2010, ApJ, 720, 1215
Rauscher, T., Heger, A., Hoffman, R. D., & Woosley, S. E. 2002, ApJ, 576, 323
Regelous, M., Elliott, T., & Coath, C. D. 2008, Earth Planet. Sci. Lett., 272, 330
Robertson, H. P. 1937, MNRAS, 97, 423
Rotaru, M., Birck, J., & Allègre, C. 1992, Nature, 358, 465
Rugel, G., Faestermann, T., Knie, K., et al. 2009, Phys. Rev. Lett., 103, 1
Russell, R. 1971, J. Geophys. Res., 76, 4949
Russell, W., Papanastassiou, D., & Tombrello, T. 1978, Geochim. Cosmochim. Acta, 42, 1075
Schönbächler, M., Lee, D., Rehkämper, M., et al. 2003, Earth Planet. Sci. Lett., 216, 467
Schönbächler, M., Rehkämper, M., Fehr, M. A., et al. 2005, Geochim. Cosmochim. Acta, 69, 5113
Schönbächler, M., Rehkämper, M., Halliday, A. N., et al. 2002, Science, 295, 1705
Shukolyukov, A., & Lugmair, G. W. 2006, Earth Planet. Sci. Lett., 250, 200
Simon, J. I., DePaolo, D. J., & Moynier, F. 2009, ApJ, 702, 707
Spyromilio, J., Meikle, W. P. S., & Allen, D. A. 1990, MNRAS, 242, 669
Steele, R. C. J., Elliott, T., Coath, C. D., & Regelous, M. 2011, Geochim. Cosmochim. Acta, 75, 7906
Tachibana, S., & Huss, G. R. 2003, ApJ, 588, L41
Tachibana, S., Huss, G. R., Kita, N. T., Shimoda, G., & Morishita, Y. 2006, ApJ, 639, L87
Tachibana, S., Huss, G. R., & Nagashima, K. 2007, in Lunar and Planetary Institute Science Conference Abstracts, Vol. 38, ^{60}Fe–^{60}Ni Systems in Ferromagnesian Chondrules in Least Equilibrated Ordinary Chondrites (Houston: LPI), 1709

Travaglio, C., Hillebrandt, W., Reinecke, M., & Thielemann, F. 2004, A&A, 425, 1029
Trinquier, A., Birck, J.-L., & Allègre, C. J. 2007, ApJ, 655, 1179
Trinquier, A., Birck, J. L., Allègre, C. J., Göpel, C., & Ulfbeck, D. 2008, Geochim. Cosmochim. Acta, 72, 5146
Trinquier, A., Elliott, T., Ulfbeck, D., et al. 2009, Science, 324, 374
Umeda, H., & Nomoto, K. 2002, ApJ, 565, 385
Wasson, J. T., & Chou, C. 1974, Meteoritics, 9, 69
Wasson, J. T., & Kallemeyn, G. W. 1988, Phil. Trans. R. Soc. A, 325, 535
Wood, J. A. 2005, in ASP Conf. Ser. 341, Chondrites and the Protoplanetary Disk, ed. A. N. Krot, E. R. D. Scott, & B. Reipurth (San Francisco, CA: ASP), 953
Woosley, S. E. 1997, ApJ, 476, 801
Wurm, G., Teiser, J., Bischoff, A., Haack, H., & Roszjar, J. 2010, Icarus, 208, 482
Yokoyama, T., O'D. Alexander, C. M., & Walker, R. J. 2010, Earth Planet. Sci. Lett., 291, 48
Yokoyama, T., Rai, V. K., Alexander, C. M. O., et al. 2007, Earth Planet. Sci. Lett., 259, 567
York, D. 1969, Earth Planet. Sci. Lett., 5, 320
York, D., Evensen, N., Martínez, M., & Delgado, J. 2004, Am. J. Phys., 72, 367
Young, E. D., Galy, A., & Nagahara, H. 2002, Geochim. Cosmochim. Acta, 66, 1095
Zinner, E. 1998, Annu. Rev. Earth Planet. Sci., 26, 147
Zinner, E. 2003, in Treatise on Geochemistry, Presolar Grains, ed. H. D. Holland & K. K. Turekian (Oxford: Pergamon), 17